Monthly Notices of the ROYAL ASTRONOMICAL SOCIETY

MNRAS **449,** 2514–2538 (2015) doi:10.1093/mnras/stv408

Calibration of the *Swift*-UVOT ultraviolet and visible grisms

N. P. M. Kuin,[1★] W. Landsman,[2] A. A. Breeveld,[1] M. J. Page,[1] H. Lamoureux,[1] C. James,[1] M. Mehdipour,[1] M. Still,[3] V. Yershov,[1] P. J. Brown,[4] M. Carter,[1] K. O. Mason,[5] T. Kennedy,[1] F. Marshall,[6] P. W. A. Roming,[7,8,9] M. Siegel,[7] S. Oates,[1,10] P. J. Smith[1] and M. De Pasquale[1,11]

[1]*Mullard Space Science Laboratory/University College London, Holmbury St. Mary, Dorking, Surrey, RH5 6NT, UK*
[2]*Space Telescope Science Institute, Baltimore, MD 21218, USA*
[3]*NASA Ames Research Center, M/ Table S 244-40, Moffett Field, CA 94035, USA*
[4]*George P. and Cynthia Woods Mitchell Institute for Fundamental Physics and Astronomy, Texas A. and M. University, Department of Physics and Astronomy, 4242 TAMU, College Station, TX 77843, USA*
[5]*Satellite Applications Catapult, Fermi Avenue, Harwell Oxford, Oxfordshire OX11 0QR, UK*
[6]*NASA Goddard Space Flight Center, Code 660, MD 20771, USA*
[7]*Department of Astronomy and Astrophysics, Penn State University, 525 Davey Laboratory, University Park, PA 16802, USA*
[8]*Space Science and Engineering Division, Southwest Research Institute, PO Drawer 28510, San Antonio, TX 78228-0510, USA*
[9]*Physics and Astronomy Department, The University of Texas at San Antonio, 1 UTSA Circle, San Antonio, TX 78249, USA*
[10]*Instituto de Astrofsica de Andalucía (IAA-CSIC), Glorieta de la Astronomía s/n, E-18008, Granada, Spain*
[11]*IASF Palermo, Via Ugo La Malfa 153, I-90146 Palermo, Italy.*

Accepted 2015 February 23. Received 2015 February 19; in original form 2015 January 12

ABSTRACT

We present the calibration of the *Swift* Ultraviolet and Optical Telescope (UVOT) grisms, of which there are two, providing low-resolution field spectroscopy in the ultraviolet and optical bands, respectively. The UV grism covers the range λ1700–5000 Å with a spectral resolution (λ/Δλ) of 75 at λ2600 Å for source magnitudes of u=10–16 mag, while the visible grism covers the range λ2850–6600 Å with a spectral resolution of 100 at λ4000 Å for source magnitudes of b=12–17 mag. This calibration extends over all detector positions, for all modes used during operations. The wavelength accuracy (1σ) is 9 Å in the UV grism clocked mode, 17 Å in the UV grism nominal mode and 22 Å in the visible grism. The range below λ2740 Å in the UV grism and λ5200 Å in the visible grism never suffers from overlapping by higher spectral orders. The flux calibration of the grisms includes a correction we developed for coincidence loss in the detector. The error in the coincidence loss correction is less than 20 per cent. The position of the spectrum on the detector only affects the effective area (sensitivity) by a few per cent in the nominal modes, but varies substantially in the clocked modes. The error in the effective area is from 9 per cent in the UV grism clocked mode to 15 per cent in the visible grism clocked mode .

Key words: instrumentation: spectrographs – space vehicles: instruments – techniques: imaging spectroscopy.

1 INTRODUCTION

The *Swift* mission (Gehrels et al. 2004) was launched to provide rapid response to gamma-ray bursts (GRB) over the wavelength range from gamma-rays to optical with three instruments: the Burst Alert Telescope (BAT) to detect gamma-rays (Barthelmy et al. 2005), the X-Ray Telescope (XRT) to observe the X-rays (Burrows et al. 2005), and the Ultraviolet and Optical Telescope (UVOT) for UV-optical photometry and spectroscopy (Mason et al. 2004; Roming et al. 2005). UVOT spectroscopy is enabled by the inclusion of two grisms, the UV grism (1700–5000 Å) and the visible grism (2850–6600 Å). These are mounted in a filter wheel which also houses the UV and visible lenticular filters.

The *Swift* grisms provide a window on the UV Universe to complement the high-resolution *Hubble Space Telescope* (*HST*) instruments with a rapid response, low-resolution option for the community. The *X-ray Multi-Mirror* (*XMM*) Optical Monitor (*XMM*-OM) (Mason et al. 2001) grisms provide a similar functionality but for somewhat brighter sources and without the rapid

★ E-mail: npkuin@gmail.com

© 2015 The Authors
Published by Oxford University Press on behalf of the Royal Astronomical Society

Downloaded from http://mnras.oxfordjournals.org/ at NASA Goddard Space Flight Ctr on November 17, 2015

response. Earlier missions which provided UV spectroscopy include the *International Ultraviolet Explorer* (*IUE*[1]) (Boggess et al. 1978) and *GALEX*[2] (Martin et al. 2003).

Since 2008 November, the automated response sequence of the *Swift* UVOT, which governs the early exposures after a BAT GRB trigger (Roming et al. 2005), has included a 50 s UV grism exposure provided the burst is bright enough in the gamma rays. So far, this has resulted in two well-exposed UV spectra of GRB afterglows: for GRB081203A (Kuin et al. 2008) and the bright nearby GRB130427A (Maselli et al. 2014). *Swift* has also obtained spectra for many other objects. These include comets (Bodewits et al. 2011), active galactic nuclei (Mehdipour et al. 2015), supernovae, e.g. Bufano et al. (2009); Brown et al. (2012) and recurrent novae (Byckling et al. 2009), where the rapid response of *Swift* has resulted in unprecedented early multiwavelength coverage.

The UVOT uses a modified Ritchey–Chrétien optical design, where light from the telescope is directed towards one of two redundant detectors using a 45° mirror. A filter wheel allows selection of either a UV or optical lenticular filter, a *white*/clear filter, a UV grism, a visible grism or a blocked position. Behind the filter wheel is an image intensifier configured to detect each photon event with a 2048×2048 pixel resolution.

The *Swift* UVOT grism filters are the flight spares for the *XMM*-OM instrument. The grisms for both instruments were designed using a Zemax[3] optical model. The *Swift* UVOT instrument design and build procedure was modified to avoid the molecular contamination which impaired the *XMM*-OM UV sensitivity. Therefore, the sensitivity of the UV grism is much better in the UV than that of the *XMM*-OM grisms. The UVOT visible grism optics were blazed at 3600 Å. However, the UVOT UV grism optics were not blazed; therefore, the second-order spectrum of this grism is significant and has to be accounted for in the analysis where the orders overlap.

Each of the two grisms can be operated in two modes. The so-called *nominal mode* is where the filter wheel is rotated so that the grism is positioned in direct alignment with the telescope optical light path. However, in order to reduce the contamination by zeroth-order emission of the background and field sources, in the so-called *clocked mode* the filter wheel is turned so the grism is partially covered by the telescope exit aperture which restricts the field of view, blocking some field stars and reducing the background light. In the clocked mode, the first-order spectra of many stars in the field of view lie in the area uncontaminated by background or the zeroth-order spectra of other field stars as shown in Fig. 1. The clocked mode has been used extensively, though the comet and GRB observations have been done in the nominal mode. A comparison of clocked and nominal images in Fig. 1 shows how effective the reduction of zeroth-order contamination is from other sources in the field for those spectra falling on the left-hand side of the image.

The detector is a Microchannel plate (MCP) Intensified Charge coupled device (CCD) or MIC (Fordham et al. 1989). Each photon incident on the S20 multi-alkali photocathode can release an electron which is amplified a million-fold using a three-stage MCP. The cloud of electrons hits a P46 fast-phosphor screen, producing photons which are fed through a fibre taper to a CCD operated in frame transfer mode. The fibre taper reduces the footprint of the image intensifier output so it fits on the exposed CCD area. The exposed area corresponds to 256 × 256 CCD pixels, but after readout the photon splash is centroided to eight times higher resolution, providing an effective image that is 2048 × 2048 pixels square. The nature of the centroiding process is such that the effective size of each of the 8×8 sub-pixels on the sky is not exactly the same, leaving a modulo-8 (MOD-8) pattern in the untreated image which can be corrected for in data processing. However, information loss that

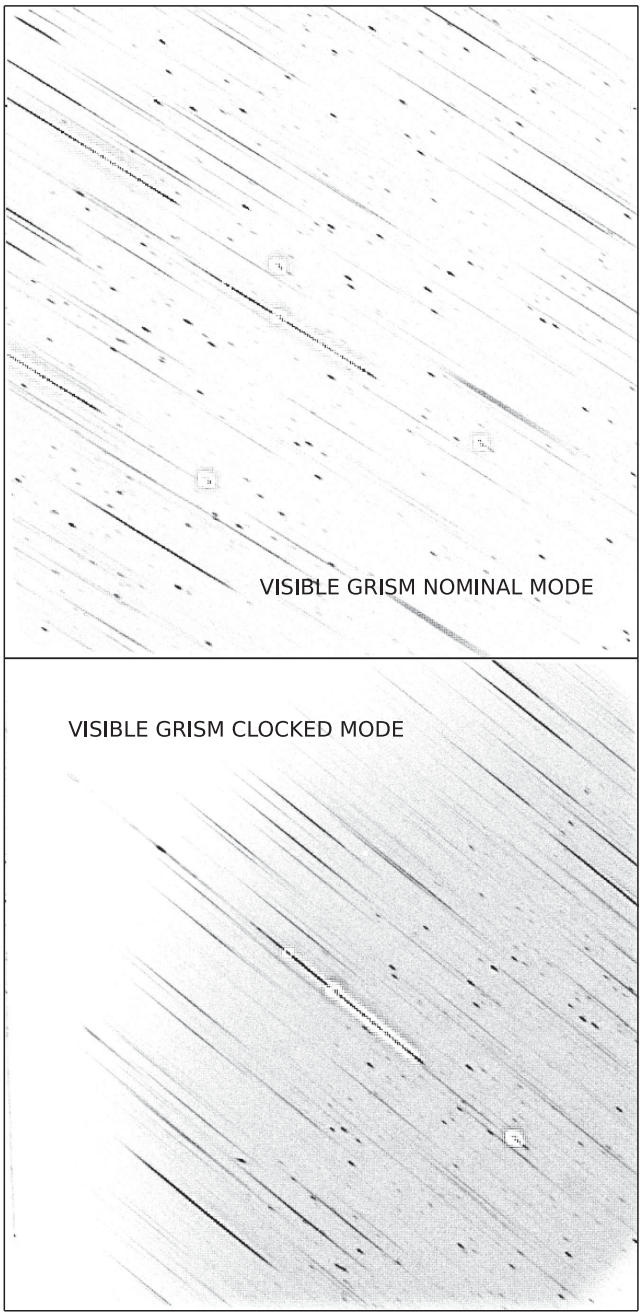

Figure 1. A typical detector image of the visible grism. The top panel was observed in nominal mode, the bottom panel in clocked mode. The zeroth orders are the short features, while the long lines are the first-order spectra. In the clocked mode, the zeroth-order images are absent from the top-left of the image. Note also the change in the angle of the spectra on the detector between nominal and clocked mode. The nominal grism image has a flat background, while in the clocked grism mode the background varies across the image.

[1] The *IUE* wavelength (two ranges 1150–2000Å; 1900–3200Å) resolution was 0.2Å for high dispersion and 6 Å for low dispersion.

[2] The *GALEX* spectral resolution ($\lambda/\Delta\lambda$) was 90 for the NUV band (1771–2831 Å) and 200 for the FUV band (1344–1786 Å).

[3] http://www.zemax.com

Downloaded from http://mnras.oxfordjournals.org/ at NASA Goddard Space Flight Ctr on November 17, 2015

Table 1. UVOT grism specifications.

	Visible grism	UV grism
Grating	300 lines/mm	500 lines/mm
Spectral resolution	100 at λ4000 Å	75 at λ2600 Å
Wavelength range (first order)	2850–6600 Å	1700–5000 Å
Wavelength accuracy (first order)	44 Å	17 (35) [f] Å
No order overlap (first order) [a]	2850–5200 Å	1700–2740 Å
Effective magnitude range [b]	12–17 mag	10–16 mag
Astrometric accuracy [c, g]	4 arcsec	3 arcsec
Scale	0.58 arcsec pixel^{-1}	0.58 arcsec pixel^{-1}
Dispersion (first order)	5.9 Å pixel^{-1} at 4200 Å	3.1 Å pixel^{-1} at λ2600 Å
Flux above which 20 per cent coincidence loss [d]	10^{-14} erg cm^{-2} s^{-1} Å^{-1}	10^{-13} erg cm^{-2} s^{-1} Å^{-1}
Zeroth-order b-magnitude zero-point [e]	17.7 mag	19.0 mag

Notes. [a]In the UV -grism, the range without second-order overlap depends on the placement on the detector.
[b]Limit depends on spectrum, see Section 11.1.
[c]Of first-order anchor point.
[d]For low backgrounds.
[e]In UV grism for 10 arcsec circular aperture centred on zeroth order after successfully correcting the astrometry.
[f]UV-grism nominal mode.
[g]Using UVOTGRASPCORR in a crowded field.

occurs when more than one photon splash is registered on a CCD pixel within the same CCD readout interval (coincidence loss) can cause some pattern to remain for bright sources after correction.

As noted above, the finite time over which each exposure is integrated on the CCD, the *frame time*, results in coincidence losses if the photon arrival rate is high enough (Fordham, Moorhead & Galbraith 2000). Statistically, there is a chance that multiple photons arrive within one CCD frame with spatially overlapping pulse profiles, in which case only one arrival will be recorded. This means that fewer source photons are detected than are incident on the detector, and the effect is larger when there is a higher input photon rate, resulting in a non-linear response with source brightness. Making use of the statistical nature of the effect, the coincidence loss can be corrected, and an expression for point sources has proved very effective in UVOT photometry, e.g. Poole et al. (2008) and Breeveld et al. (2010). Extremely bright sources, above the brightness limit for coincidence loss correction, suffer a further loss due to interference from events registered in neighbouring CCD pixels.

The background due to dark current in the detector is very low; instead the sky background is the limiting factor for faint sources. The sky background in the grisms is comparable to that in the UVOT white (clear) filter since both grisms transmit the 2800–6800 Å optical band.

The sensitivity of the UVOT lenticular filter exposures is decreasing slowly with time. In the UV filters the loss is about 1 per cent per year (Breeveld et al. 2011), while in the v-band optical filter it is larger, 1.5 per cent per year.[4] Most likely ageing of the MCPs (proportional to lifetime photon throughput) is the main cause of the decreasing sensitivity which will affect all filters equally, while aging of the filter itself explains the different rate in the v-filter. The 1 per cent sensitivity decrease is assumed to apply when the grism is employed as well as the lenticular filters and is used for the grism calibration and data reduction.

The grism image is usually stored as an accumulated image on board the spacecraft, although it is also possible to record the data as an event list of photon times and positions. After transmission to the ground, the data are routinely processed into raw images, which are corrected for the MOD-8 pattern, followed by a correction due to small distortions in the fibre taper[5] into a *detector image*. The detector image is the basis for the spectral extraction.

Knowledge of the position of the spectrum on the detector is crucial for determining the wavelength scale. The UVOT spectra are formed by slitless dispersion such that the detector position depends on the position of the source on the sky. To define the position of the spectrum on the detector, we use the position of a particular wavelength in the first order, referred to as the *anchor position*. The anchor position in the visible grism is found at 4200 Å, in the UV grism at 2600 Å.

Table 1 provides a summary of the capabilities of the grisms. More details can be found in the main body of the paper.

The rest of this paper is organized as follows: first, we provide more details on the UVOT grisms and the optical model, and discuss the appearance of the grism spectrum on the image. We discuss how we map the sky position to that of the anchor point of the spectrum on the image. Next we discuss the calibration of the dispersion. Then we present our correction for the coincidence loss in the spectra and we determine the effective areas by including the coincidence loss corrections. After discussing the second-order effective areas, we consider the zeroth-order effective area and derive a photometric method and zero-point for the UV grism. Next follows a description of the method used for extracting the spectra, and the related software. We conclude by describing how to use the UVOT grism, and some additional information that can be useful for the user.

In the following, we use the term *default position* for the spectrum placement in the middle of the detector, roughly at the boresight of the instrument. This is the normal operating position for sources; other positions are at an *offset*. The term *anchor* is used to designate the position that fixes the wavelength scale, in that the dispersion is measured relative to that position. By *model* we mean the Zemax optical model, either corrected or not.

[4] Updates to the UVOT calibration documents are at http://heasarc.gsfc.nasa.gov/docs/heasarc/caldb/swift/

[5] the fibre taper distortion correction was determined using the lenticular filters

Downloaded from http://mnras.oxfordjournals.org/ at NASA Goddard Space Flight Ctr on November 17, 2015

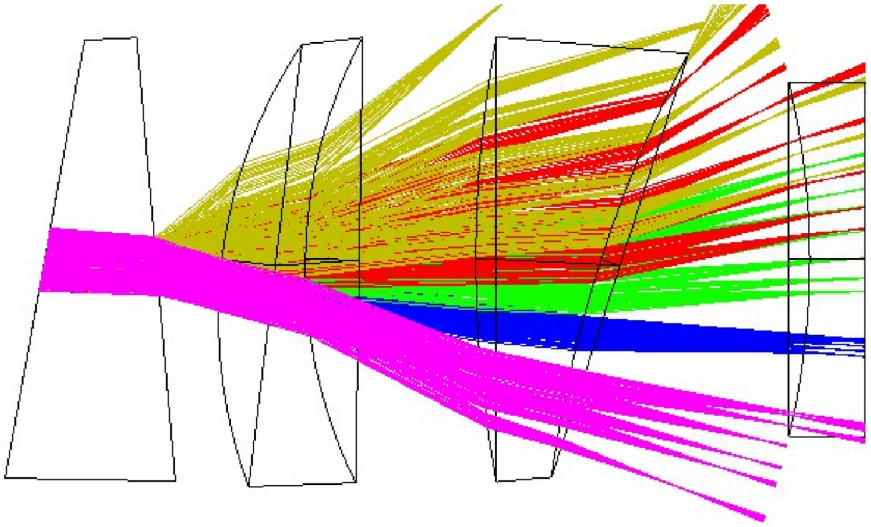

Figure 2. Optical schematic of the UVOT UV -grism with rays for multiple wavelengths and orders -1(pink), 0(blue), +1(green), +2(red) and +3(orange). The computation was made for an on-axis beam coming in from the left, while it ends on the right at the entrance of the image intensifier. The green rays in the centre are of the UV part of the first order. Long wavelengths of the first order can be seen interleaved with red second and orange third-order rays.

2 DESCRIPTION OF THE GRISMS AND THE OPTICAL MODEL

The 'grisms' are actually made up of two optical elements: a grism and a tilt compensator as shown in Fig. 2. The grism provides on-axis dispersion by means of a prism and transmission grating, but the focal plane is tilted. The tilt compensator element flattens the focal plane. The UV grism is direct ruled on a *Suprasil* substrate, while the visible grism is replicated *epoxy*. The grating in the visible grism is blazed to maximize the transmission of the first order. The UV grism grating was not blazed. Because the optics are in the converging beam of the telescope, which uncompensated would induce a shift in focus, the leading surface is slightly convex. The dispersed light is refocussed before leaving the grism. The grism design was optimized for the UV grism in the first order around λ2600 Å, and in the visible grism around λ4200 Å.

The Zemax model which was used to design the grism optics has been used to assist in the in-orbit grism calibration, but some adjustments were needed. A significant reason for adjustment is that the model does not include the fibre taper optics between the MCP and the CCD (Roming et al. 2005), and that the glass catalogue of the model does not include coefficients for the refractive elements below 2000 Å. The optical model was modified for the clocked modes with an appropriate decenter and rotation around the optical axis of the grism assembly.[6]

The boresight of the model was aligned to the observed boresight for all modes, but then a further adjustment of (−60,0) pixels was needed for the UV grism to align the model drop in flux in the left top corner of the detector due to the clocking to match the observations from calibration spectra.

The optical model predicts that the point spread function (PSF, which describes the distribution of where monochromatic photons fall on the detector) increases in size in the UV grism towards the red. This is illustrated in Fig. 3, where the two-dimensional model PSF has been integrated normal to the dispersion, illustrating the PSF variation as a function of wavelength.

[6] The rotation is called a 'tilt' in the Zemax model.

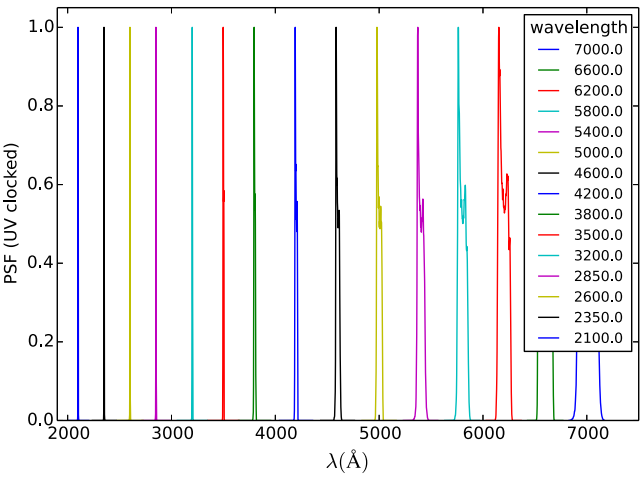

Figure 3. The model point spread function of the UV grism is illustrated as a function of wavelength.

The large width of the PSF in the UV grism for wavelengths longer than 4500 Å causes the spectrum to appear smoothed out with wavelength at these wavelengths. In the UV, despite the small PSF width predicted by the model, other factors contribute to broadening the spectrum. Specifically, the actual PSF below 3000 Å is thought to be dominated by the transverse spreading of the electrons leaving the cathode. Spacecraft jitter during the observation is removed using the shift and add method (Roming et al. 2005). This results in a full width at half-maximum (FWHM) of the PSF of typically 3 pixels, about 10 Å, in the UV part of the spectrum in the UV grism and about 20 Å in the visible grism.

Fig. 2 displays a UV grism model calculation for an on-axis source of the rays for several UV wavelengths and for the five orders that can be registered on the detector. The first, second and third orders overlap, while the zeroth and minus-first orders are separate.

The model zeroth-order spectrum is dispersed in a hyperbolic fashion, as discussed in more detail in Section 9.1. As a result photons with wavelengths longer than about λ3500 Å fall within a single pixel and in the UV grism, the UV spectrum forms a very

Downloaded from http://mnras.oxfordjournals.org/ at NASA Goddard Space Flight Ctr on November 17, 2015

weak tail that extends for 200 pixels, see for example the inset in Fig. 5.

The dispersion angle, or slope of the spectra in the detector image, varies by about 5 degrees over the detector for a given mode. The angle near the centre of the image is different for each mode due to the positioning of the grism in the filter wheel and filter wheel clocking, and is 144°.5 (UV grism clocked mode), 151°.4 (UV grism nominal mode), 140°.5 (visible grism clocked mode), and 148°.1 (visible grism nominal mode).

The model predicts the variation of the dispersion angle over the detector, but does not include the curvature of the spectra in the UV grism. The predicted model dispersion angle is used in the spectral extraction; see Section 10.

3 THE APPEARANCE OF THE SPECTRUM ON THE DETECTOR

The appearance of the grism spectrum differs between the UV and visible grisms. This applies equally to nominal and clocked modes in the same grism.

In both grisms, the zeroth order extends over several pixels, and the higher orders overlap. However, in the visible grism the zeroth-order brightness and second-order brightness are much less than the first order. As a result, the contamination of the first-order spectrum from higher order light is small, and contamination by zeroth orders of field stars is usually small. The spectral tracks in the visible grism are straight, which means the spectrum is easy to extract. The angle of the spectra in the detector frame varies slightly over the detector, however. Example images are shown in Fig. 1.

The zeroth and second order in the UV grism are of comparable brightness to the first order, see Fig. 7. Like in the visible grism the zeroth order is extended, with a very small tail due to the UV response, and the first and higher orders tend to overlap. Unlike the visible grism, the UV part of the spectrum in each order is generally curved. The curvature is largest in the upper right and lower left corners of the detector image and goes in the opposite direction. The spectral track is straight near the centre of the image, where there is full overlap of first and second orders. Depending on where the spectrum falls on the detector, the second-order overlap can start in the first order as soon as 2740 Å or as late as 4500 Å. A simplified drawing of the layout of the UV grism image can be found in Fig. 4.

The appearance of the observed curvature and displacement in the UV grism is evident in images with a very bright source, e.g. Fig. 13. The magnitude of the effect is a function of detector position, being very small at the default position. Adopting a straight line in the dispersion direction as reference, the maximum curvature offset in the cross-dispersion direction varies from about 16 pixels in the lower left up to minus 25 pixels in the top right hand detector corner.

In the visible grism, there is no noticeable curvature or any offset of the higher orders at any point on the detector.

3.1 Bright sources

One of the characteristics of the grism images is that there is a MOD-8 pattern of dark (low count rate) pixels next to the spectra of bright sources; see for example the nominal mode UV grism image of the region around WR52 in Fig. 5, with the highlighted WR52 spectrum in the centre. The cross-hatched MOD-8 pattern is a sign that coincidence loss is present in the spectrum. Even when it is present, a correction for the coincidence loss is often still possible.

For sources with a *b* magnitude brighter than about 17 the zeroth order in the UV grism develops a dark patterned region because of coincidence loss, and when brighter than 13th magnitudes, a region with a 49 pixel radius around the source is affected and can cause part of a nearby spectrum to be unreliable.

Occasionally, very bright stars ($V < 8$th mag) are in a grism image. These can cause problems because their readout streak (caused by exposure of the column during the image transfer to the CCD readout area) leads to columns of elevated counts across the image, e.g. Page et al. (2013). When the readout streak crosses a spectrum, it does so at an angle and background subtraction and the correction for coincidence loss may be affected.

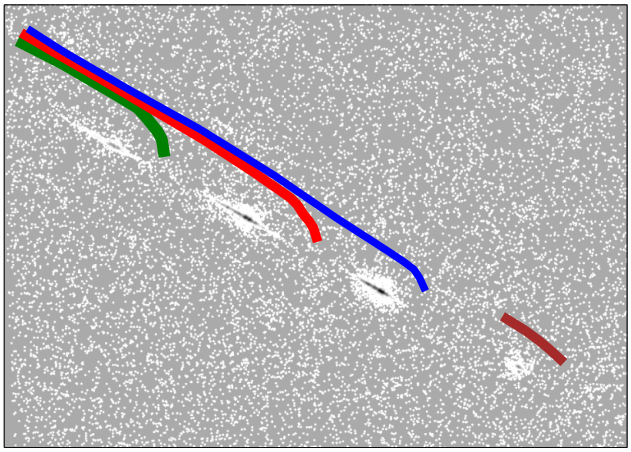

Figure 4. A section of a ground calibration image of a narrow band filter exposure around 260 nm in the UV grism outlines the positions of the orders. A cartoon of the typical relative positions of the spectral orders is shown above the data. The first order in blue, the second order in red, the third order in green and the zeroth order in brown. The curvature of the spectral orders, which only occurs in the UV grism has been exaggerated for illustration.

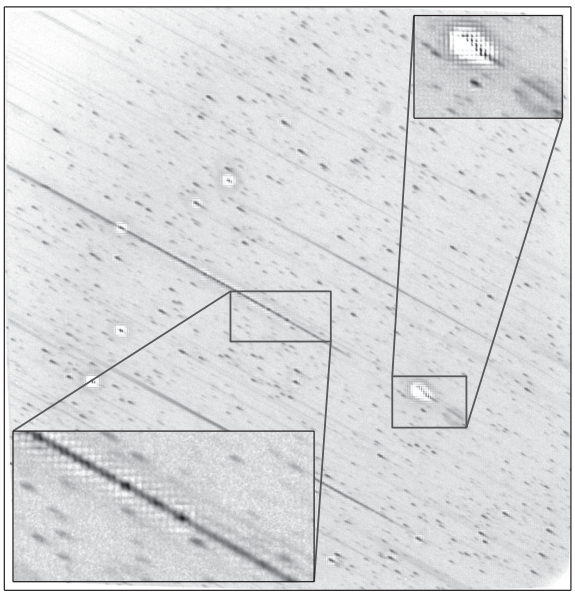

Figure 5. A typical detector image of the UV grism in nominal mode. The top inset highlights the extended disconnected UV -tail in the zeroth order of the UV-bright source in the centre. The disconnection is due to a combination of detector effective area and interstellar extinction. The background around the bright zeroth order has been eaten away due to coincidence loss, and shows up as white pixels. The bottom inset shows the MOD-8 pattern around a bright spectrum. Notice the many zeroth orders from weaker sources.

Downloaded from http://mnras.oxfordjournals.org/ at NASA Goddard Space Flight Ctr on November 17, 2015

In parts of calibration spectra brighter than the coincidence-loss upper limit of 5 counts per frame, a smaller count rate is observed than the expected count rate of nearly 1. This is thought to be caused by the amplified photon splash saturating neighbouring pixels. This would cause the centroiding to fail in which case those events are not counted. However, at such brightness the coincidence loss distorts the source spectrum severely so confusion with the spectrum of a fainter source is unlikely.

Other features due to scattered light that are seen in the lenticular filter images (Breeveld et al. 2010) may also be present in grism images. Experience shows that they do not occur frequently enough to affect the grism spectroscopy in practice.

3.2 The fibre taper distortion

Images taken through the UVOT lenticular filters are spatially distorted by the image intensifier and fibre taper, with a small contribution from the lenticular filter itself. The correction has been determined to be the same for all lenticular filters, so a single distortion correction is needed to map positions on the detector to those on the sky. Using this distortion map, the standard ground processing produces a corrected image called the *detector image*.

The grism causes further distortion and this might be wavelength and order dependant.

In order to do the anchor point calibration, we need to correct for the distortion of the anchor points, so we can find a mapping from the sky position to the anchor position. We also need to map the zeroth-order positions so we can get an astrometric solution for the grism image.

The same distortion map as used for the lenticular filters is used to convert the raw grism image to a detector image. It takes out the major distortion due to the image intensifier and fibre taper, though it may overcorrect somewhat since it also includes the lenticular filter part of the correction.

The model predicts the grism distortion, so it theoretically could be used to do the mapping from sky to anchor position after correcting for the image scaling caused by the fibre taper. However, the model does not predict this distortion completely accurately. Some differences remain from the observed anchor positions which are considered likely to be due to the unknown overcorrection due to the lenticular filters.

The distortion in the detector image of the zeroth-order positions due to the grism optics was calibrated using catalogue positions of the `USNO-B1` catalogue for several fields, and is made available[7] in the *Swift* CALDB.[8]

3.3 The cross-dispersion profile

The final footprint of the light entering the detector is primarily broadened by transverse diffusion of the electron cloud in the gap between the cathode and MCP, which has a profile similar to a Gaussian. The grism optics also add broadening so that the spectral profile is of different width for the different orders. Finally, coincidence loss further affects the profile.

In the UVOTPY software (see Section 10), a fit is made of the count rate as a function of pixel distance to the centre of the track using a Gaussian distribution

$$f(x) = a\, e^{-(\frac{x-x_0}{\sigma})^2} \quad (1)$$

[7] swugrdist20041120v001.fits
[8] http://heasarc.gsfc.nasa.gov/docs/heasarc/caldb

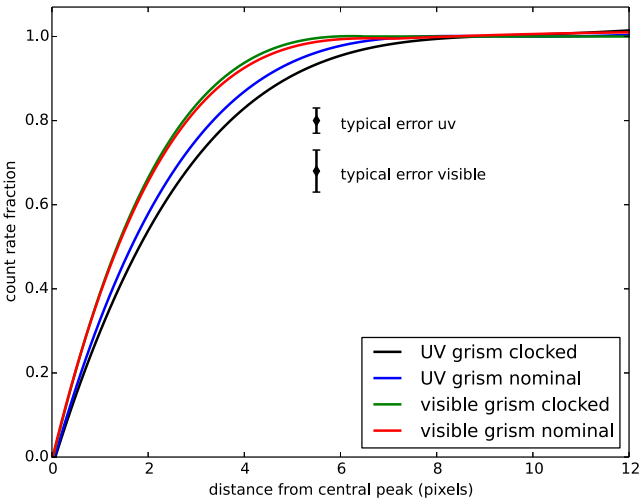

Figure 6. The cross-dispersion count rates within a slit as function of the pixel distance to the centre of the spectral track level off around 7.5 pixels in the UV grism, and around 5.5 pixels in the visible grism. The profiles shown are for weak spectra with the lowest possible coincidence loss (WD1657+343).

with x, the cross-dispersion pixel coordinate, a the peak count rate, x_o the centre of the spectral track and σ controls the width of the Gaussian fit.

In the first-order UV grism, σ is about 2.9 pixels at 1700 Å, growing to about 3.3 pixels at 6000 Å. The second order is broader, with $\sigma \approx 4.5$ pixels wide. The values are slightly smaller for the visible grism, at 2.7 pixels.

Measurements were made of the profile normal to the dispersion, which we will call the *cross-track* profile. The measurements were made in the region of no-order overlap by repeatedly extracting the spectra with varying extraction widths. The cross-track profile is not completely Gaussian, but falls off more steeply in the wings. The plot of the enclosed count rates, similar to encircled energy in a point source but for a linear feature (see Fig. 6) shows the cumulative distribution starting from the centre as a function of the pixel distance from the centre to the border of the extraction 'slit'. The width of the spectral track is seen to be smaller for the visible grism than for the UV grism. This profile can be used as an aperture correction, see Section 11.2.

The width of the spectral track changes with increasing coincidence loss due to the developing MOD-8 pattern. This variation introduces an uncertainty larger than 20 per cent in the aperture correction when the coincidence loss is more than 20 per cent. Therefore, a smaller aperture for the spectral extraction with aperture corrections should only be used for faint spectra.

4 CALIBRATION APPROACH

Before a full calibration of the wavelength and flux could be attempted, we needed to have a good aspect correction for the grism images so we know the sky location of the boresight, and measure the width and curvature of the spectra over the detector. These basic calibrations were done first.

We have adopted an approach which merges the calibration observations with the grism Zemax optical model. The optical model uses the optical set-up to predict the dispersion, order overlap, PSF, and throughput, and predicts their variation as a function of the source position in the field of view. The model contains a major part

Downloaded from http://mnras.oxfordjournals.org/ at NASA Goddard Space Flight Ctr on November 17, 2015

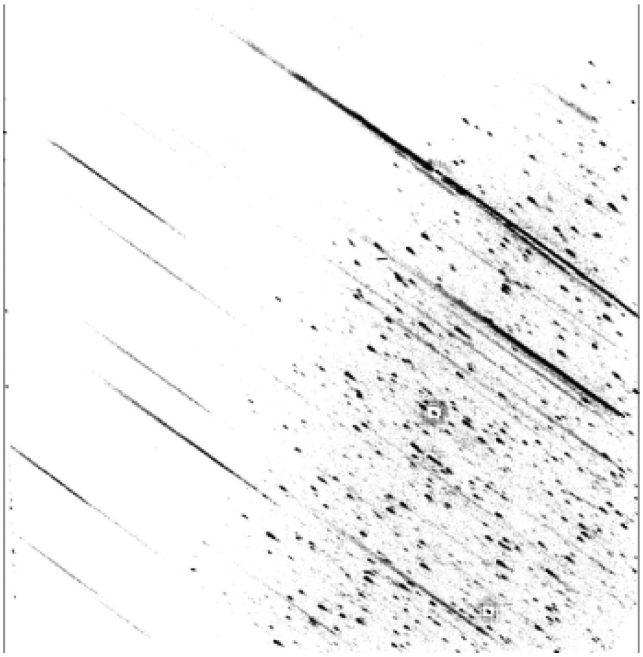

Figure 7. A typical detector image of the UV grism in clocked mode.

of the physics of the optics and thus it constrains the calibration, provides a way to verify observed parameters, and allows us to extend the calibration to all parts of the detector. As a result we can have a more reliable calibration by determining corrections in the form of alignments and by scaling the model where appropriate.

4.1 Method of implementation

For the UV wavelength calibration sources, we selected Wolf–Rayet (WR) stars with a fairly good coverage of bright emission lines in the UV; see Table 2. These sources are on the upper range of brightness that can be observed with the UVOT grisms. For the calibration of effective area and coincidence loss, we used mainly sources with reference spectra in the CALSPEC[9] data base which are flux calibrated to typically 2–3 per cent.

We selected anchor positions for this calibration at 2600 Å for the UV grism and 4200 Å for the visible grism in the *first* order. Therefore, the anchor position on the detector is similar to the position of the source in the raw image in a lenticular filter when taken alongside the grism exposure.

The curvature was measured relative to the model dispersion angle for the first and second orders for all UV grism calibration spectra and a correction was derived, expressed in terms of polynomials. The polynomial coefficients vary with the anchor position of the spectrum but the curvature is always the same in the same grism mode at the same detector position. Bisplines were fitted to the polynomial coefficients, which allow the retrieval of the curvature at any anchor point on the detector. The coefficients of the curvature calibration have been implemented in the UVOTPY software (Kuin 2014), see Section 10. The spectra in the visible grism are not measurably curved, but straight.

The variation of the width of the first and (where possible) second spectral order was determined in the UV grism and also compared from image to image. Because of width variations along the spectrum, the spectral extraction was designed to keep the same enclosed energy for a consistent flux calibration by adjusting for slow variations in the width of the spectrum during spectral extraction.

Once we understood broadly the geometry, for each grism mode the analysis of anchor position, dispersion, coincidence loss and effective area was repeated as discussed in the next sections.

5 CALIBRATION OF THE ANCHOR POINT

5.1 The astrometric correction of the grism image

The aspect is initially corrected using the best attitude from the spacecraft which is accurate typically to within 1.3 arcsec (1σ); see Breeveld et al. (2010).

The positions of weak zeroth orders can be used to derive an improved aspect solution. The aspect correction is done by applying the UVOTGRASPCORR *ftool* [10] which uses the appropriate distortion file from the *Swift* CALDB described previously in Section 3.2. The aspect corrected coordinates are written to the FITS header as the WCS-S world coordinate system keywords including the keywords for the Simple Imaging Polynomial convention (Shupe et al. 2005) which capture the zeroth-order anchor distortion.

The accuracy of the astrometric correction depends on the success of the UVOTGRASPCORR program. In the visible grism, with weaker zeroth orders due to the blazing, the errors tend to be larger. These are reported in terms of the anchor point accuracy in Table 3, and in the middle panel of Figs 8, 10, 11 and 12. The results show a scatter that varies mainly by target, while for a given target different images tend to have similar errors. Tests show that the program fails in 3–4 per cent of the fields, in which case the correction can still be done by hand.

5.2 Reference data

The anchor and wavelength dispersion calibration consists of the determination of the scaling of the model by using calibrated spectra of bright WR stars.

Our WR stars were observed by *IUE*, and have also ground-based spectra available with sufficiently good wavelength calibration to determine the wavelengths of spectral emission lines. Major lines used in the WC-type spectra are Si II 1816 Å, C III 1909 Å, 2297 Å, C IV 2405, 2530, 2906 Å, O IV 3409 Å, C III 4069, 4649 Å and C IV 5801 Å, while for the WN-type spectra we used He II 2511, 2733, 3203, 4686 Å. Further minor emission lines, sometimes blended, are present in our spectra. For WR121, which was used for the visible grism, no *IUE* spectrum is available, but for the same spectral type the *IUE* spectrum of WR103 provides a similar spectrum with the line identifications from Niedzielski & Rochowicz (1994) and a good ground-based spectrum from Torres & Massey (1987). For WR4, no ground-based spectrum was used, but the lines were easily identified from comparison to the other spectra. Though WR86 is a binary, the spectrum is dominated by the WC spectrum; radial velocities may lead to shifts of <2 Å which are negligible at the resolution of the grisms.

For the wavelength verification, some spectra from the flux calibration sources were used. The lines used in those spectra are mainly Mg II 2800 Å and the hydrogen lines.

[9] http://www.stsci.edu/hst/observatory/cdbs/calspec.html

[10] http://heasarc.gsfc.nasa.gov/docs/software/ftools/

Downloaded from http://mnras.oxfordjournals.org/ at NASA Goddard Space Flight Ctr on November 17, 2015

Table 2. Calibration targets used.

Name/ID	Sp. type	J2000 RA	Position DEC	Used for	Reference spectrum, notes
WR1	WN4	00:43:28.4	+64:45:35.4	1	*IUE*, *
WR4	WC5+?	02:41:11.7	+56:43:49.7	1	*IUE*
WR52	WC4	13:18:28.0	−58:08:13.6	1	*IUE*,#
WR86	WC7(+B0III-I)	17:18:23.1	−34:24:30.6	1	*IUE*,#
WR121	WC9d	18:44:13.2	−03:47:57.8	2	*IUE*, $
WD0320−539	DA	03:22:14.8	−53:45:16.5	3,4,5	CALSPEC
WD1057+719	DA1	11:00:34.2	+71:38:03.9	3,4,5	CALSPEC
WD1657+343	DA1	16:58:51.1	+34:18:53.5	3,4,5	CALSPEC
GD153	DA1	12:57:02.3	+22:01:52.7	5	CALSPEC
GSPC P177-D	F0V	15:59:13.6	+47:36:41.9	3,4,5	CALSPEC
GSPC P 41-C	F0V	14:51:58.0	+71:43:17.4	3,4,5	CALSPEC
BPM16274	DA	00:50:03.7	−52:08:15.6	4,5	ESO *HST* standards
GD108	sdB	10:00:47.3	−07:33:31.0	4,5	CALSPEC
GD50	DA2	03:48:50.2	−00:58:32.0	4,5	CALSPEC
LTT9491	DB3	23:19:35.4	−17:05:28.5	4,5	CALSPEC
WD1121+145	sdB	11:24:15.9	+14:13:49.0	3,4,5	CALSPEC
G63-26	sdF	13:24:30.6	+20:27:22.1	3,4,5	STIS-NGSLv2
AGK+81 266	DB2	09:21:19.2	+81:43:27.6	5	CALSPEC
BD+25 4655	DB0	15:51:59.9	+32:56:54.3	5	CALSPEC
BD+33 2642	B2 IVp	15:51:59.9	+32:56:54.3	5	CALSPEC
Use:	(1) UV grism anchor and wavelength calibration.				
	(2) Visible grism anchor and wavelength calibration				
	(3) UV grism flux calibration				
	(4) visible grism flux calibration				
	(5) coincidence loss calibration				
CALSPEC	The *Hubble Space Telescope* calibration spectra data base at STScI				
IUE	ESA Vilspa archive for the *International Ultraviolet Explorer*				
*	Hamann, Koesterke & Wessolowski (1995)				
$	Torres & Massey (1987), used WR103 to ID lines				
#	CDS catalogue III/143 Torres-Dodgen & Massey (1988)				
	spectral types from van der Hucht (2001), Cooke & Sion (1999), CALSPEC.				
STIS-NGSLv2	http://archive.stsci.edu/prepds/stisngsl/				
ESO *HST* standards	http://www.eso.org/sci/observing/tools/standards/spectra/hststandards.html				

Table 3. Default anchor positions and wavelength accuracy.

Grism mode	Anchor[a] default position	Anchor 2σ accuracy(Å) detector centre[b]	Wavelength accuracy(Å)[c] detector centre[b, d]	Anchor 2σ accuracy(Å) full detector	Wavelength accuracy(Å)[c] full detector
Anchor position determined using a mode combined with lenticular filter					
UV nominal	[1005.5,1079.7]	30	7,18,36	35	8,16,34
UV clocked	[1129.1,1022.3]	12	8,11,21	17	7,22,18
visible nominal	[1046.3,1098.3]	30	5,10,6	44	6,13,6
visible clocked	[1140.7,1029.6]	48	5,14,13	44	4,13,12
Anchor position determined using astrometry from UVOTGRASPCORR					
UV nominal	[1005.5,1079.7]	53	46,15,22	53	51,17,25
UV clocked	[1129.1,1022.3]	47	8,11,21	47	7,12,18
visible nominal	[1046.3,1098.3]	88	3,10,8	88	5,13,7
visible clocked	[1140.7,1029.6]	118	9,16,14	118	8,16,12

Notes. [a]First order, in detector coordinates
[b]The detector centre is defined by image pixels between 500 and 1500 in X and Y.
[c]Excluding errors due to the anchor.
[d]2σ errors for three ranges in the UV grism of $\lambda < 2000$ Å, $2000 < \lambda < 4500$ Å, 4500 Å $< \lambda$, and in the visible grism of $\lambda < 3100$ Å, $3100 < \lambda < 5500$ Å, 5500 Å $< \lambda$.

Downloaded from http://mnras.oxfordjournals.org/ at NASA Goddard Space Flight Ctr on November 17, 2015

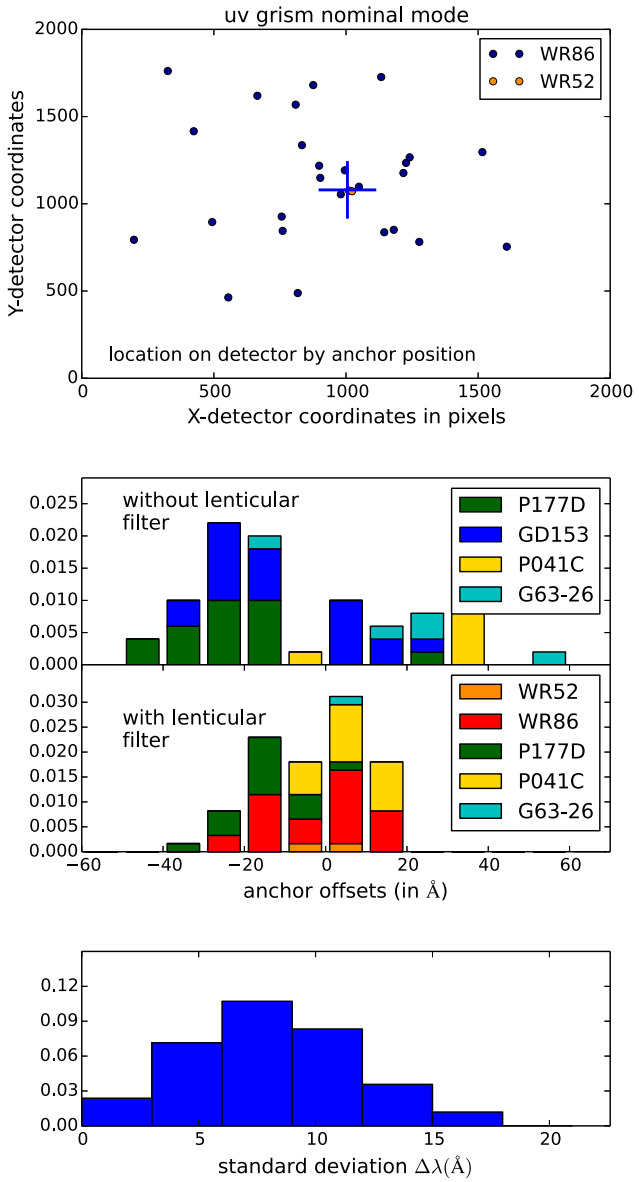

Figure 8. The anchor and wavelength calibration for the UV grism nominal mode . The top panel shows the positions on the detector for each spectrum used in the wavelength calibration. The position of the anchor for a spectrum at boresight is indicated with a blue cross. The second panel shows the measurement of the wavelength shift due to errors in the anchor position for two methods, by using UVOTGRASPCORR, and with a lenticular filter alternatively. The third panel shows the histogram of the standard deviation of the errors in the measured wavelengths after removing the anchor error.

5.3 First order anchor position – fitting to model

In order to calibrate the anchor position, calibration spectra accompanied by an image in a lenticular filter were taken of WR stars, see Table 2, while the pointing was offset so that the spectra covered the detector; see the top panels in Figs 8, 10, 11 and 12, where the locations of the anchor points on the detector are plotted. Although the emission lines in these stars are broad, their width is not an impediment as it is close to the spectral resolution of the instrument.

The calibration spectra were observed in a special mode, where a lenticular filter exposure is taken just before and/or after the grism exposure. The spacecraft pointing is not changed during the

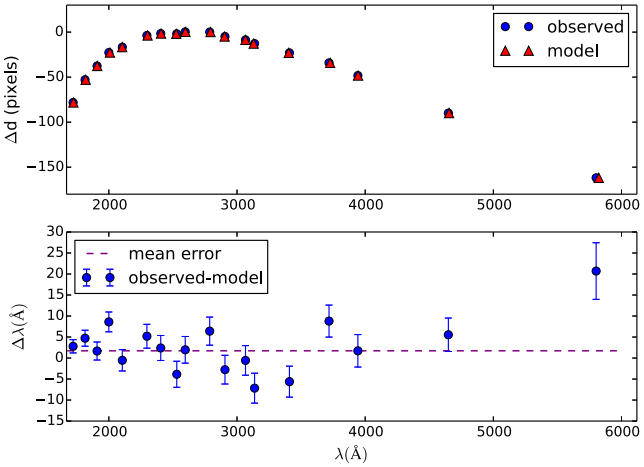

Figure 9. Example of the determination of the wavelength accuracy for one calibration spectrum in the clocked UV grism. In the upper panel, Δd is derived from the anchor distance in pixels, after subtracting a linear constant dispersion factor, and illustrates the higher order variation of the dispersion. The lower panel shows the errors in the measured wavelengths.

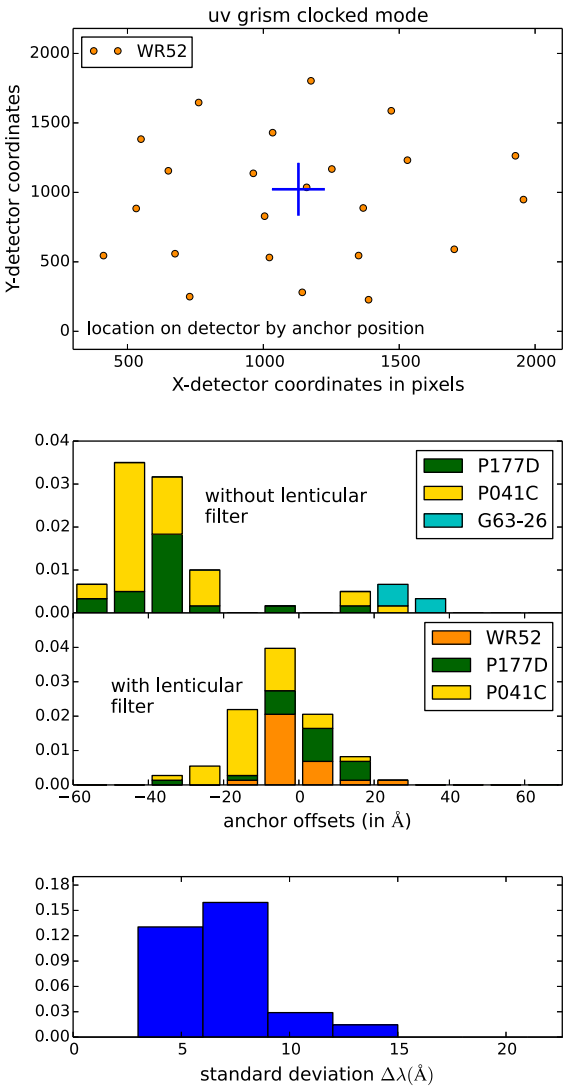

Figure 10. Accuracy of the wavelength calibration for the UV grism clocked mode . See Fig. 8 for explanation of each panel.

Downloaded from http://mnras.oxfordjournals.org/ at NASA Goddard Space Flight Ctr on November 17, 2015

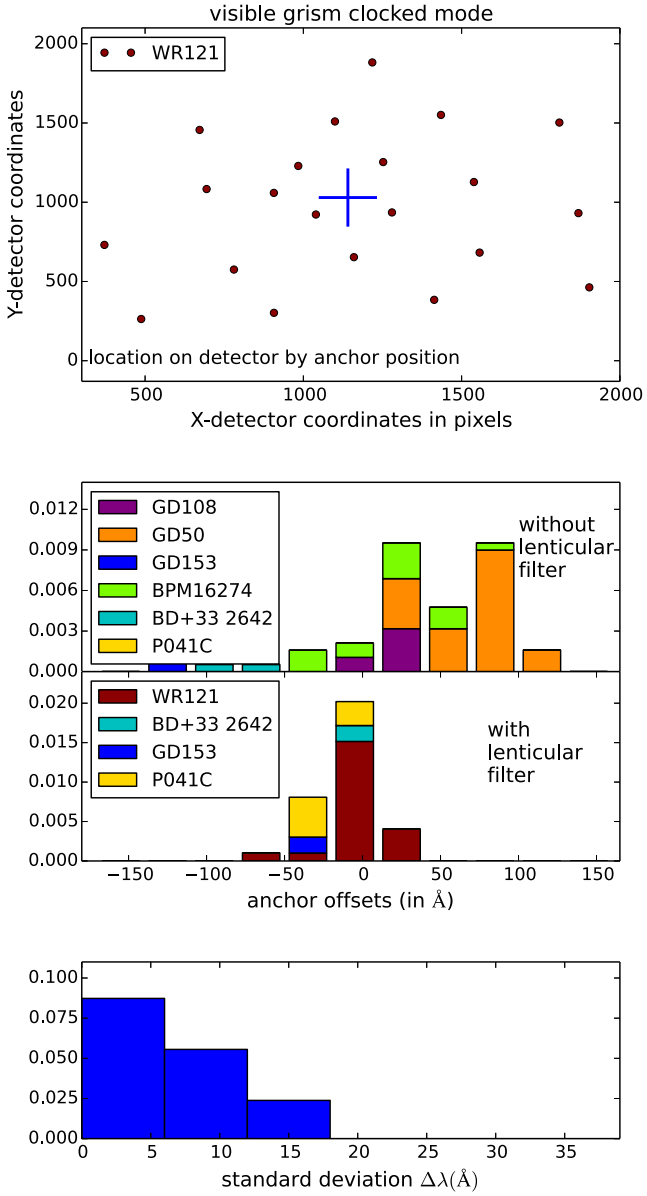

Figure 11. Accuracy of the wavelength calibration for the visible grism clocked mode, see Fig. 8. See Fig. 8 for explanation of each panel.

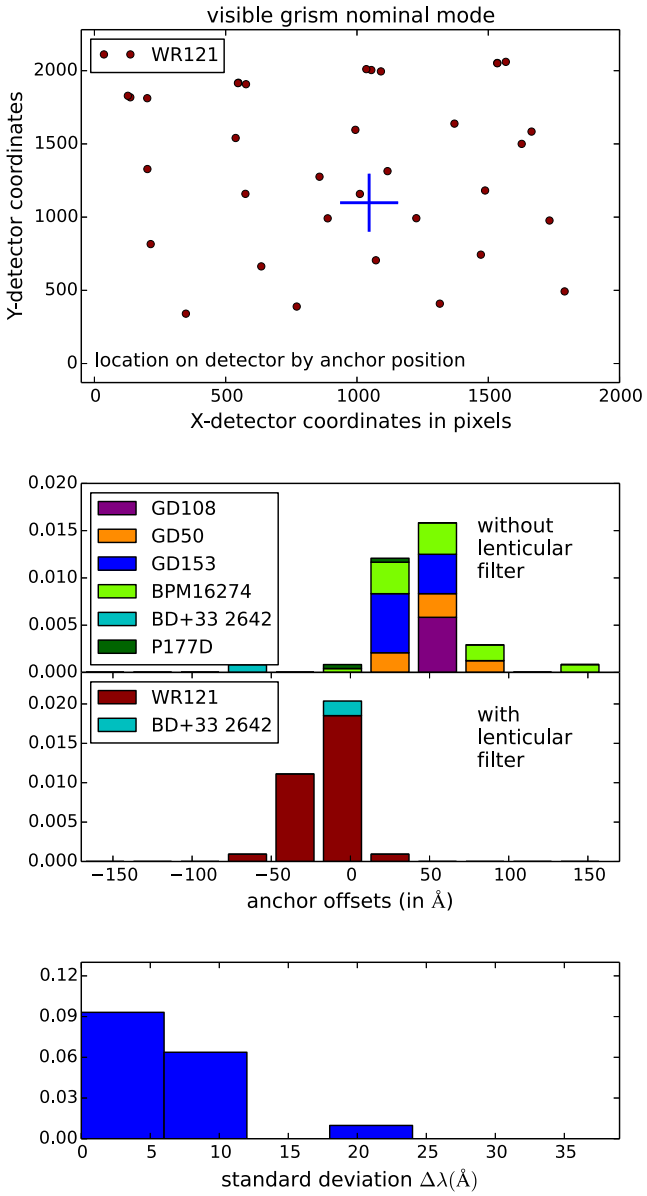

Figure 12. Accuracy of the wavelength calibration for the visible grism nominal mode, see Fig. 8. See Fig. 8 for explanation of each panel.

sequence although there may still be some drift in the pointing between the exposures. Within an exposure, the positions are corrected using the on-board shift-and-add algorithm (Poole et al. 2008). The position of the target in the lenticular images can then be correlated to that of the observed anchor in the grism.

The position of the source relative to the boresight in the lenticular image and the anchor position relative to the boresight in the grism image are related in a fixed manner. Ignoring the distortion, the conversion from lenticular filter to grism position is a shift in detector X,Y position and a scale factor. No rotation is necessary, due to the coordinates being tied to the detector orientation.

For each observed spectrum, bright spectral lines were identified in the image close to the anchor point, whereafter the anchor point on the detector image was determined for each spectrum. The anchor positions for the default position (with the source at the boresight) have been given in Table 3 in *detector coordinates*,[11] and are shown in the top panel in Figs 8, 10, 11 and 12 as a blue cross.

A comparison of the observed grism anchor positions and source positions in the corresponding lenticular filter(s) implies a pixel scale in the grism image of 0.58 ± 0.04 arcsec pixel^{-1}, larger than the 0.502 value for the lenticular filter, though it should be noted that the pixel scale varies due to distortion.

In the lenticular image, the position of the source can be found from the sky position. Given the source sky position and the FITS WCS header in the aspect corrected lenticular filter image, we derive the astrometrically corrected source position on the lenticular filter image and thus the source position relative to the boresight position;

[11] The detector coordinates are converted here from mm to pixels by a centre of [1100.5,1100.5], and a scale factor of 0.009075 mm/pix.

Downloaded from http://mnras.oxfordjournals.org/ at NASA Goddard Space Flight Ctr on November 17, 2015

that relative position is converted into the field coordinate[12] for input to the model. We now can use the model to find the anchor position on the grism detector image, provided the model has been properly scaled.

We found that a simple scaling of the pixel size in the model brought all the model and observed anchor positions to within 16 pixels. The position differences were not displaced randomly, so a bispline fit to the X and Y coordinate differences provided a final correction. The order of the bisplines was kept as small as possible in order to keep the number of parameters low.[13]

The corrected model was used to tabulate a lookup table of anchor positions on a grid of field positions. The lookup table was used subsequently to rederive the anchor positions to obtain an estimate of the accuracy.

Any inaccuracy of the anchor position leads to a shift in the wavelength scale. Since many calibration observations had a lenticular filter before and after the grism exposure, we also obtained an estimate of the pointing drift during the exposures (often 1 ks long) of typically 6 pixels (≈3 arcsec), though a larger excursion between exposures (10 pixels) was observed in a single observation. This is consistent with the accuracy seen in the anchor positioning. In the UV grism nominal mode, calibration there was only one lenticular filter in the observation so no correction for drift between the grism and lenticular filter exposure was possible. This explains the larger errors in the anchor position calibration (thus the wavelengths were shifted more).

Calibration observations taken before 2008 did not include a lenticular filter. This includes most of the flux calibration spectra for the visible grism. When using the sky position from the image header to determine the anchor position without using a lenticular filter image taken next to the grism image, the anchor error is due to the accuracy of the UVOTGRASPCORR program as discussed in Section 5.1 above.

Verification with independent data was done using flux calibration targets with good enough spectral lines. The anchor offset was determined for the case that a lenticular filter was used for determining the anchor position, and also by using the UVOTGRASPCORR program. The wavelength calibration sources were not considered, since they were already used to determine the mapping from the first-order boresight to the zeroth-order boresight position (used in the grism WCS-S). The middle panels in Figs 8, 10, 11 and 12 show histograms of the measured corrections to the wavelengths, taken at the anchor position. The corrections derived for independent sources when using the lenticular filter method show a similar distribution as the WR sources used for the wavelength calibration. The corrections derived when not using a lenticular filter show a much larger spread. In particular for the visible grism, an apparent bias in the offset appears. This is due to there being a large number of spectra taken under similar observing conditions for some sources which give a consistent offset for that single source. The derived accuracy is reported in Table 3. For the case of anchor position without a lenticular filter, the uncertainties are considered to be the same over the whole detector.

[12] The field coordinate is the angular coordinate relative to the boresight.

[13] For example, for the UV grism clocked mode, there were 24 parameters used to fit 50 positional data; other grism modes used fewer parameters to fit a comparable number of data points. Therefore, enough free parameters remain.

5.4 Second-order anchor position

The WR calibration sources have bright lines, and using the model as guidance, the much weaker second-order UV lines were identified in the UV grism calibration images. In the visible grism, the orders are weaker and overlap and this is not possible. There the model prediction was used.

Similar to the first order, we define an anchor position in the second order at a fixed wavelength. For the calibration, we determine the distance of the second-order anchor to that of the first order. Errors in the first-order anchor position are easier to correct that way than by working directly with the second-order position on the image.

Using the observable lines in the UV grism, an anchor position of λ2600 Å in second order was determined by interpolation, and sometimes extrapolation, as well as a scaling factor for the second-order spectral dispersion for the areas on the detector where there was not much overlap of first and second order.

The distance of the first- and second-order anchor was thus derived. No scaling of the model was attempted on the first- to second-order distances which were fitted with a bispline instead. By interpolation, we obtain a prediction of the anchor position for the area of complete order overlap. The main source of error in the second-order parameters is the error in the first-order anchor position.

6 THE DISPERSION OF THE SPECTRA

6.1 The method used

For the anchor position calibration, the anchor in each spectrum had already been determined by examining the position of the nearby lines on the image. We could consider the positions of the other lines in the image relative to that anchor and compare to the predicted positions from the Zemax model.

The comparison showed that a scaling had to be applied to the model to properly fit the observed spectral line positions in the calibration spectra. For each spectrum, the pixel position of lines relative to the anchor position were measured, while the wavelengths were taken from line identifications and/or the reference spectrum. The measured wavelengths are affected by the MOD-8 noise from coincidence loss because the calibration sources are very bright, which leads to a measurement error of about one pixel, except for wavelengths in the UV grism above 4800A, where the error is slightly larger, see Fig. 9.

The Zemax model calculations were made on a 28 × 28 grid of positions on the detector, referenced by the anchor position. Each model spectrum was computed at a range of wavelengths. The same wavelengths were used in all spectra for the UV grism, and a second set was used for all spectra computed for the visible grism. In order to interpolate the dispersion from the model, for the UV grism a fourth order and for the visible grism a third-order polynomial were fitted to the model. To determine the dispersion at any point on the detector, for each polynomial power, the polynomial coefficients of the nearest model grid points are interpolated using bilinear interpolation. Initially, this was used to determine a model dispersion at the actual position of the calibration spectrum.

The dispersion relation as determined from the Zemax model calculation was compared to the observed line positions to refine the scaling factor needed for the model. There is some spread in the difference between model and observed line positions. Using all lines in a spectrum, the rms of the errors in the line positions is

Downloaded from http://mnras.oxfordjournals.org/ at NASA Goddard Space Flight Ctr on November 17, 2015

used as a measure of the accuracy of the dispersion. This was used iteratively to improve the scale factor used in the model.

The resulting rms error for all spectra, which cover the face of the detector by position in each grism and mode, have been shown as histograms in the bottom panels of Figs 8, 10, 11 and 12. The mean values of rms are given in Table 3.

The best-fitting scale factor to the dispersion is close to a single value for the whole detector for each mode. However, some fine adjustments were necessary. As noted in Section 2, the glass catalogue of the model did not include coefficients for the refractive elements below 2000 Å, which were extrapolated. Also, the very extended nature of the PSF above 4500 Å in the UV grism may lead to a different interpretation of the emission line peak location in the model and observed line positions.

The lowest order acceptable fits were adopted. In the dispersion calibration for the UV grism nominal mode only a constant was needed for an acceptable fit, but in the visible grism nominal mode a bilinear fit was needed. In the UV grism clocked mode a linear-quadratic fit, and in the visible grism clocked mode a bilinear fit were adopted. The UV grism clocked mode also includes a linear dispersion scaling (i.e. it includes a wavelength-dependent factor).

Finally, using the scaled model obtained as described above, dispersion polynomial coefficients were tabulated for a 28 × 28 grid covering the detector. This allows for accurate interpolation at any anchor location. The table was written to the wavelength calibration file, one for each grism mode.

6.2 Internal accuracy of the wavelength scale

We next verified the dispersion. In order to verify the accuracy of the dispersion calibration file, we should have used independent observations. However, this would require a prohibitive amount of extra observing time. We have used only a limited number of parameters to perform the model scaling and thus using the calibration observations (which have two to three times as many parameters) should give a valid indication of the accuracy of the calibration.

While the calibration software accessed the Zemax model and applied the required scaling, for the verification we used the calibration file with the UVOTPY software (see Section 10).

As an example of an individual spectrum, Fig. 9 displays in two panels the wavelength accuracy. After taking out the linear term of the dispersion, the remaining variation in the dispersion shows small offsets between the values from the spectral extraction (observed) and those determined by careful calibration (model). The positions of spectral lines were taken from our calibration data and compared with the position predicted by the dispersion relation for that spectrum for those lines. This is presented in the bottom panel which shows as a function of wavelength the standard deviation of the difference $\Delta\lambda$ between predicted and measured wavelengths.

The total wavelength error varies over the detector and is smallest near the default position.

6.3 Wavelength calibration of the second order

The second order in the visible grism is weak, since the grism was blazed, and has not been considered for calibration.

In the UV grism, the second order separates from the first order most prominently in the upper right hand part of the detector. Fig. 13 shows an annotated section of a grism image of a bright WR star. Compare also to Fig. 4 for a cartoon schematic. The [1600,1440] anchor position shows that the spectrum is in the upper right hand corner of the image.

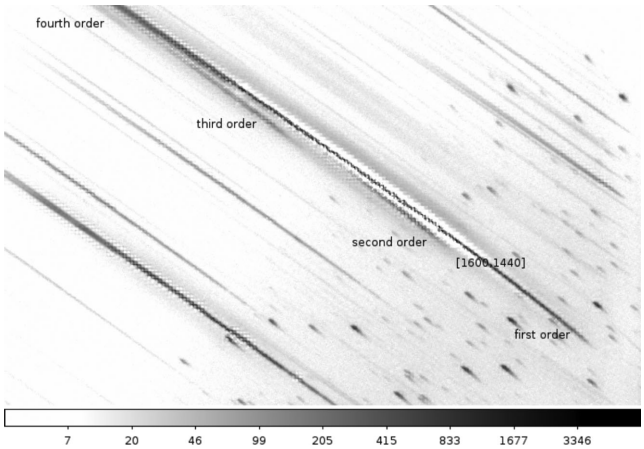

Figure 13. Section of the UV grism image containing a very bright source spectrum in the top right corner. Here the first order is overwhelmed by coincidence loss related MOD-8 patterning and the higher orders clearly separated from the first order. The approximate anchor position is indicated as coordinates.

As mentioned in Section 5.4, the spectral lines in the WR calibration spectra were used. The model predicts the second order, but the order distance and dispersion need to be scaled, just like for the first order. The 1909 Å line is usually seen clearly. In second order, the stronger lines at 2297, 2405 and 2530 Å fall close to the very strong 4650 Å first-order line, which complicates their identification. The 3409 Å line is sometimes visible where the first order is tapering off, and adds a useful data point for the dispersion.

This calibration was done for both UV grism modes, resulting in a solution for the second-order dispersion. The predicted positions for the UV grism clocked mode are within 50 Å. The main reason for a large error seems to be that any error in the anchor position affects the second order scale nearly twice as much.

The first- and second-order overlap starts at different wavelengths depending on the position of the spectrum on the detector because of the curvature. Even at large offsets the second-order and first-order converge at longer wavelengths. That means that only the UV part of the second order is useful. For the best case, at an anchor offset from the default position on the detector of $\Delta x > 2'$, $\Delta y > 4'$ the second order from 1700 to 2200 Å will be unaffected by the first order, and will not contaminate the first order up to wavelengths of about 4500 Å.

Fig. 14 shows the first and second orders for the bright star WR52. The second-order position relative to the first order was used when extracting the spectrum. The second order is extracted using this position which partly overlaps the first order. Therefore, when the location of the second-order extraction slit falls over the first order, the combined counts are obtained. Once this happens the plot shows a falsely brighter second order. The same is done for the first order. In the region of overlap, the effective areas of first and second order are different which accounts for the different derived flux in 'first' and 'second' order in the region of overlap. It can also be seen that in the region of order overlap the bright second-order UV emission lines of 2297, 2405 and 2530 Å marginally affect the first-order spectrum. The second-order contamination is larger when the spectrum is brightest in the UV (see also Section 8.4).

Downloaded from http://mnras.oxfordjournals.org/ at NASA Goddard Space Flight Ctr on November 17, 2015

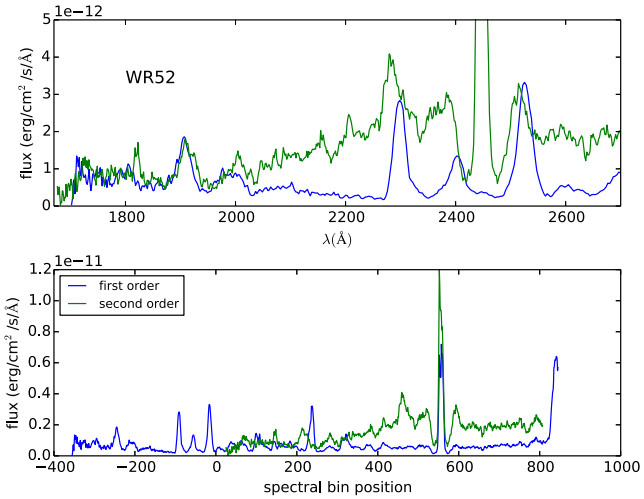

Figure 14. First and second orders when the spectrum is at an offset from the default position (anchor position = [1480,1490]). The bottom panel plots the spectra as a function of position on the detector, while the top panel shows them as a function of wavelength. The second order merges with the first order above 2000 Å in second order. In the bottom panel, you can see that the second order is influenced by the bright first-order 4649 line Å. When plotted in wavelength it is not so obvious. The second-order lines at 2297, 2405 and 2530 Å are bright enough to slightly affect the first order.

7 COINCIDENCE LOSS CORRECTIONS

In Section 1, we introduced the way the detector works, and the resulting potential for coincidence loss. Due to the finite number of frames in any measurement the statistics follow a binomial distribution. Therefore, the general form of coincidence loss for a point source can be determined as a function of the incident count rate and a correction factor can be applied.

The geometry of the spectrum on the detector is different from that of a point source but, since the statistics are similar, the same approach can be taken. To account for the difference in geometry, the area on the detector for calculating coincidence loss has to be adjusted.

The in-orbit effect of coincidence loss on high backgrounds was investigated for background and point sources in Breeveld et al. (2010), who showed that the correction used for point sources was good for the typical backgrounds in UVOT photometry. The spectra of the faintest sources have count rates that are smaller than the background rate. Therefore, we can safely assume that the coincidence loss correction formulated for the background will give the right correction for the faint spectra. This approach was used to derive the initial coincidence loss correction for UVOTPY software version 1.

7.1 The nature of coincidence loss in spectra

As mentioned in the introduction, the finite frame time t_f (typically 0.0110329 s) of the UVOT MIC detector places limits on the ability to detect high count rates C_r (in counts per second), since each detection area can only measure one count per frame. Let us define the counts per frame by the Greek letter φ, which is then found from

$$\varphi = C_r t_f, \tag{2}$$

where C_r and t_f were introduced previously. The count rate is computed using a certain area on the detector as discussed below. The incident counts on the detector are assumed independent so that an exposure of N frames has a binomial distribution which in the limit of a large number of frames turns into a Poisson distribution. Accounting for the fact that coincidences of multiple photons in a frame are only counted as one, the statistics then relate the measured counts per frame, defined as φ_m, to the incident counts per frame, defined as φ_{in}. For a simple point source, the statistical relation is given by

$$\varphi_{in} = \frac{-1}{\alpha} \quad ln(1 - \varphi_m), \tag{3}$$

where α is the fraction of the frame time when the frame is exposed, excluding the dead time for CCD frame transfer, and ln is the natural logarithm. For the default UVOT full-frame readout $\alpha = 0.984$. It has been assumed in this paper that the measured count rate has already been corrected for dead time, similar to the usage in Poole et al. (2008).

Coincidence loss tends to steepen the PSF in point sources, and Poole et al. (2008) found that an aperture of radius 10.5 ± 1.2 pixels gave the optimal aperture range where photometry was the least affected by coincidence loss. Hence a circular aperture with a radius of 10 pixels was chosen for the detection area for UVOT photometry in the lenticular filters. However, a circular area is not appropriate for the grism spectra. A different area for coincidence loss must be determined.

The idea of a coincidence area was proposed by Fordham et al. (2000) to explain that the coincidence loss they found for flat-field illumination of the detector was larger than that in a single pixel. Using an appropriate coincidence area for determining the count rate, they showed that the relation from equation (3) also applied to the flat illumination. We therefore explored a coincidence loss area for correcting the grism spectra.

In spectra, the detector illumination extends over many pixels, far more than the three used in the centroiding of events. This will tend to increase the coincidence loss. The physical reasoning behind this is that the centroiding of a photon splash in a frame will pick the highest peak. Statistical noise, and the linear spectrum in the grism images implies that in some frames neighbouring pixels will have more chance to cause coincidence loss than would happen in a point source. Based on this simple picture we would expect a larger coincidence loss area for grism spectra than for a point source.

Some new questions arise that were of no concern for a point source or even background illumination. One such question is how far the effects of coincidence loss reach along and across the spectrum? How should we interpret the extent along the spectrum over which the coincidence loss works in a bright emission line? That distance may be an indication of the extent of the coincidence loss area along the spectrum.

When we consider the spectra of a series of sources with increasing brightness, it becomes clear that spectra exceeding a certain brightness level show instrumental peaks and valleys. It is thought that the high brightness affects the on-board centroiding which has been fine tuned for a smoother brightness variation. The photons at high coincidence loss are mis-registered and appear as bright points in a MOD-8 pattern in the grism image. As the spectrum lies at an angle over the pixel grid, the brightness distribution of the extracted spectrum of a very bright source shows this variation, even when the source spectrum is smooth. This effect is most prominent at the bright part of the spectrum where the grism effective area peaks. For example, spectra taken from GD153, a DA white dwarf star, see Fig. 15 show this. That spectrum is quite typical for the variations

Downloaded from http://mnras.oxfordjournals.org/ at NASA Goddard Space Flight Ctr on November 17, 2015

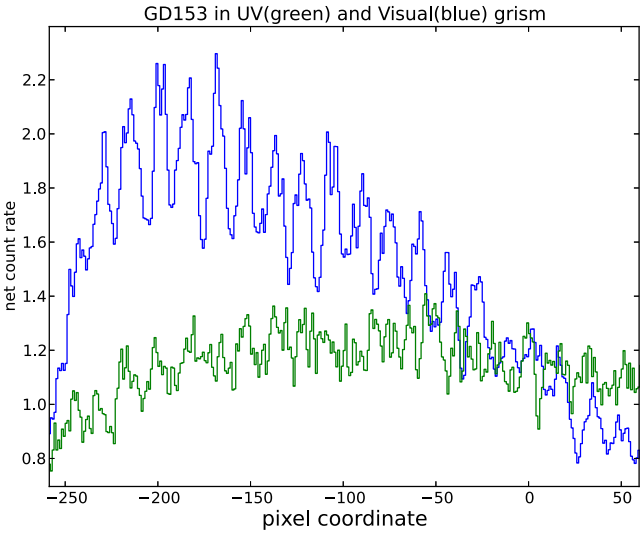

Figure 15. The effect of coincidence loss on a smooth input spectrum. The blue spectrum shows GD153 in the visible grism, the green spectrum in the UV grism.

in spatial frequency. The pattern is more pronounced in the visible grism since it is more sensitive than the UV grism.

For the determination of the coincidence loss, we need to average over this pattern and this pattern determines the minimum length along the spectrum that we need to include. Bright spectral lines show that the coincidence loss is quite extended. After some trials, we decided to use a length $L_{\rm coi}$ along the spectrum determined as 24 subpixels divided by the cosine of the typical angle of the spectrum on the detector for each of the grism modes. This averages the count rate over most of the variations.

The coincidence area $A_{\rm coi}$ is most simply represented by a box of length $L_{\rm coi}$ and width $W_{\rm coi}$, multiplied with a correction factor $m_{\rm coi}$, named coi-multiplier,

$$A_{\rm coi} = L_{\rm coi} \times W_{\rm coi} \times m_{\rm coi}. \quad (4)$$

The measured count rate for the coincidence loss correction is thus determined for that area, and the corresponding background is computed for an equivalently sized area.

Equation (3) defines a relation between the observed count rate and the actual photons incident on the detector. We used sources with a known spectrum to fit the data to the theoretical relation in order to determine the best coi area width and the corresponding coi-multiplier. Data from multiple sources were used to increase the range of brightnesses.

For studying the coi-effect, the spectra were split into adjacent areas extending over a length $L_{\rm coi}$. A range of width $W_{\rm coi}$ were chosen. For each area, the average observed count rate was determined. That count rate differs from the count rate determined within the aperture of the spectrum, as it is used for calculating a correction factor for the coincidence loss only. We refer to this as the 'observed coi count rate'.

The sources that were used have been listed in Table 2. Bad areas of the spectra were filtered out, and areas of possible second-order overlap were removed. All spectra were in the central area of the detector (800 × 800 pixels).

The reference calibration spectrum of each source is then used as follows to find a predicted count rates: (i) Using the observed spectrum, wavelength ranges for each coi-area are determined. (ii) The spectral dispersion is used to convert the flux per angstrom in the reference spectrum to the flux per channel in the coi-area. (iii) The effective area is used to convert to count rate per channel.

Table 4. Coincidence loss area box length and width.

Grism mode	$L_{\rm coi}$ pixels	$W_{\rm coi}$ pixels	coi-multiplier $m_{\rm coi}$
UV nominal	27	15	1.12±0.05
UV clocked	29	15	1.11±0.05
Visible nominal	28	14	1.13±0.03
Visible clocked	31	13	1.09±0.03

Theory tells us that the maximum observed rate per frame approaches one asymptotically.[14] For that reason, we observed some sources that were bright enough to reach the limit. The grism images of these sources exhibit the MOD-8 pattern in the spectrum, and although they need to be 'averaged' over the coi-box, are good enough to determine the coincidence loss. In point sources, incident count rates of 3.5 counts per frame leads to an observed rate per frame of 0.97. This is considered to be the practical limit for a good measurement. For the grisms, we see similar numbers, but for this analysis incident count rates per frame of up to 5.5 were included. For each coi width $W_{\rm coi}$ the optimal value for the coi-multiplier was determined using a least-squares fit on the individual data points and the χ^2 of the fit was computed. We also grouped the data per source, and calculated the coi-multiplier for each source by inverting equation (4). Outliers were clipped in both calculations, and data at the ends of the spectra, which have less sensitivity, were also not used. Both methods prefer small widths for $W_{\rm coi}$ and similar coi-multiplier $m_{\rm coi}$ for each grism mode, see Table 4. The error on $m_{\rm coi}$ found from the individual least-squares fit was an order of magnitude smaller than the error on $m_{\rm coi}$ derived after determining a coi-multiplier per source. We attribute that to systematic errors in the measured count rates that depend on things such as how crowded the field of the calibration source is.

For the best-fitting values of $W_{\rm coi}$ and $m_{\rm coi}$, we plot in Figs 16, 17, 18 and 19 the total observed count rate per frame as function of the predicted count rate per frame, where the predicted count rate per frame from the source includes the observed background count rate per frame corrected for coincidence loss using equation (3) using the same coi-area. The observed count rates level off to a rate of 1 count per frame when the incident counts per frame reach around 4 to 5. The values found for *AGK+81 266* tend to be offset from the other data, like *BD+33 2642* which may be due to nearby spectra of bright field stars in their images.

For continuum sources, the coincidence loss affects the shape of the spectrum once the incident counts per frame exceed 1, i.e. photons are not measured at the right wavelength due to the centroiding error at high illumination.

To apply the coincidence loss correction to the flux, we determine for each channel by what factor, called the coi-factor $f_{\rm coi}$, the measured net count rate needs to be multiplied as follows:

$$f_{\rm coi} = \frac{\varphi_{in}}{\varphi_m}. \quad (5)$$

For determining $f_{\rm coi}$, φ_m is found by measuring the count rate in the coi-area multiplied by $m_{\rm coi}$ (see equation 4) and φ_{in} is then

[14] Very bright sources with incident count rates per frame larger than 6 suffer additional losses when the detector PHD saturates in neighbouring pixels.

Downloaded from http://mnras.oxfordjournals.org/ at NASA Goddard Space Flight Ctr on November 17, 2015

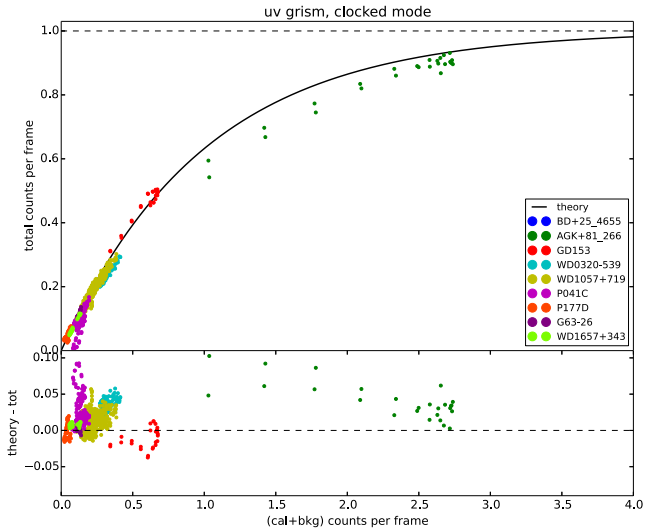

Figure 16. The coincidence loss in the UV grism, clocked mode. Using our calibration sources we can find the count rate per frame expected to be incident to the detector and plot the observed count rate per frame as function of the expected rate. The observed rate is the sum of source and background and so we also add the observed background to the predicted rate to be consistent. This plot shows the best fit of the observations to the relation of equation (3) using the parameters in Table 4

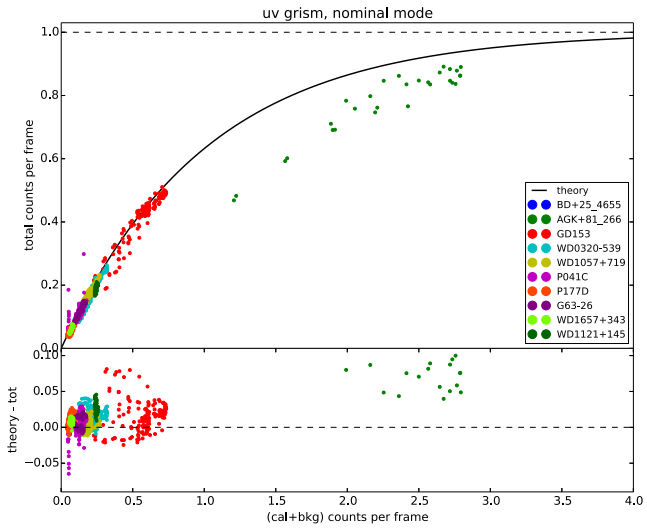

Figure 17. The coincidence loss in the UV grism, nominal mode. See the caption of Fig. 16.

derived using equation (3). For each spectrum channel this factor is computed.

Once the count rate in a channel of the spectrum is measured using a width expressed in terms of σ (equation 1) as described in Section 3.3, it is multiplied by the coi-length, the coi-multiplier, and an appropriate aperture correction. Finally, we find the incident, coi-corrected count rate for that channel by multiplying the result with $f_{\rm coi}$.

Fig. 20 shows the UV spectra after the coi correction has been applied, where they are compared to the reference spectra. In Fig. 21, a similar comparison is made using the calibration spectra in the visible grism.

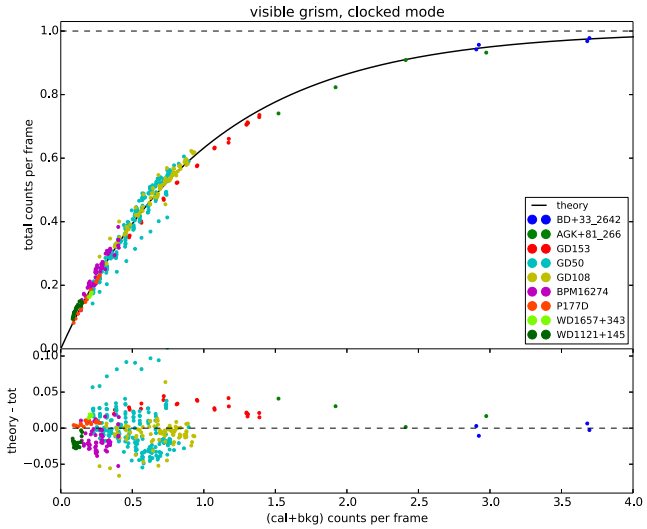

Figure 18. The coincidence loss in the visible grism, clocked mode. See the caption of Fig. 16.

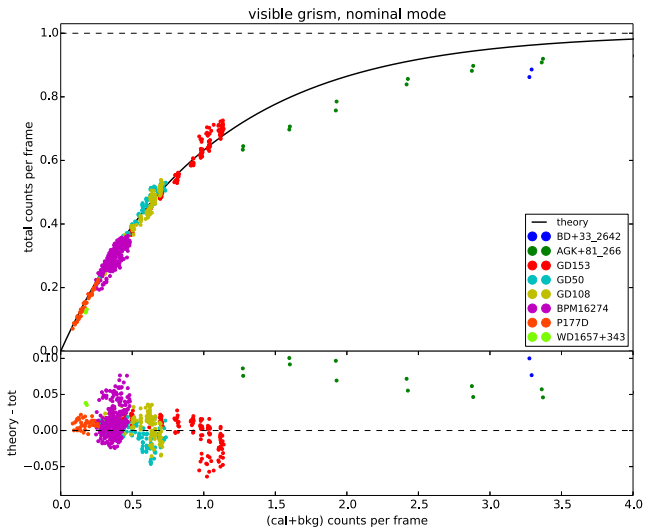

Figure 19. The coincidence loss in the visible grism, nominal mode. See the caption of Fig. 16.

8 DETERMINATION OF THE EFFECTIVE AREA

The conversion from measured count rates to flux is done by expressing the detector sensitivity as an *effective area* which depends on the wavelength. The effective area $A_{\rm eff}$ is defined as follows:

$$A_{\rm eff} = \frac{hc}{\lambda} \times \frac{C_r^{in} \times r(t)}{F_{\rm cal} \times (\Delta\lambda/bin)}, \tag{6}$$

here h is Plancks constant, c the velocity of light, λ the wavelength. The $(\Delta\lambda/bin)$ factor is derived from the dispersion relation. The known flux $F_{\rm cal}$ is obtained from the source listed in Table 2. C_r^{in} is the observed source spectrum count rate per spectral bin after correcting for coincidence loss and subtracting the coi-corrected background by using equation (5), i.e. the true count rate incident on the detector. $r(t)$ corrects for the sensitivity loss of the detector over time, taken to be 1 per cent yr^{-1}.

Downloaded from http://mnras.oxfordjournals.org/ at NASA Goddard Space Flight Ctr on November 17, 2015

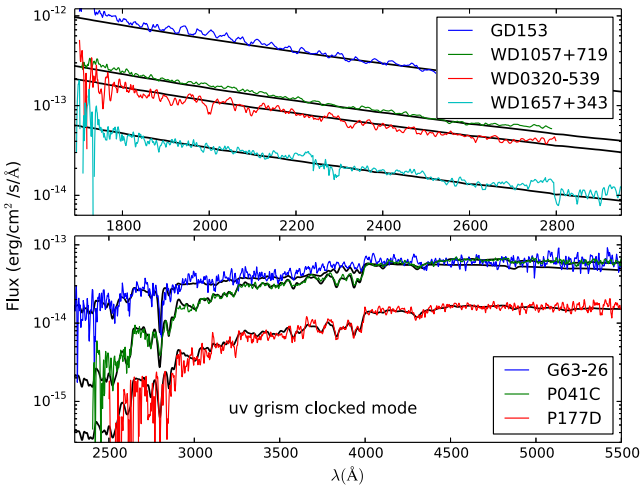

Figure 20. Observed, coincidence loss corrected, spectra in the UV grism clocked mode . The black lines are for the reference spectra. The top panel shows three white dwarfs of a range of brightness, the bottom panel one F0V subdwarf, and two main sequence solar-type stars. The spectra are the weighted average of spectra from 2–7 exposures. Coincidence loss varies from 4 per cent to about 70 per cent.

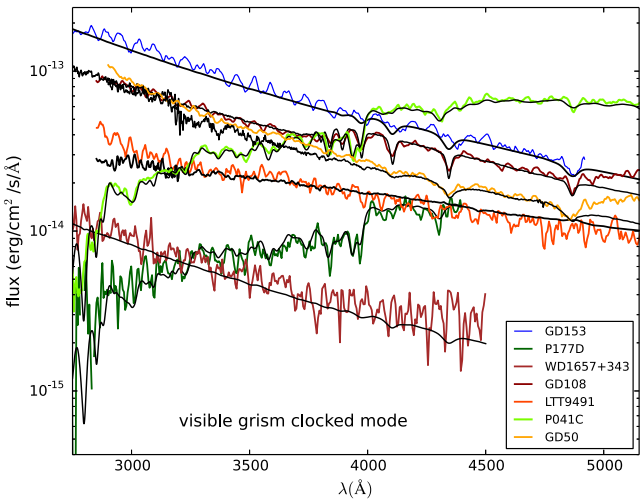

Figure 21. Observed, coincidence loss corrected, spectra in the visible grism clocked mode. The black lines are for the reference spectra. The P177D and WD1657+343 spectra are from single exposures; the other spectra are weighted averages from multiple exposures. The second order affects the spectra above $\lambda = 5200$ Å, and is more pronounced for the brighter spectra. The GD153 spectrum is distorted by spatial MOD-8 effects of the coincidence loss and illustrates the effective brightness limit. GD50 which is slightly less bright is also affected to some extent.

8.1 The effective area for the centre of the detector

In order to determine the effective area, the calibration sources in Table 2 were observed several times for each grism mode, but in various detector locations. The count rate spectra were extracted with a 2.5σ spectral track width (see discussion in Section 11.2), following the curvature of the track. Where spectral order overlap would be an issue, the data were discarded. Areas affected by underlying zeroth orders of field stars were also discarded, as well as spectra which had another first order of a different field star overlapping. For a good effective area, we need both a blue star and a red star spectrum. The second order in the red spectrum sets in at a much longer wavelength and therefore allows the determination of the effective area to longer wavelengths. In practice, in the UV grism, the white dwarf spectra were thus used typically for wavelengths of λ1650–2900 Å, and spectra from the *F*0 stars for λ2900–5000 Å and in the visible grism the WD spectra up to 4900 Å and the *F*0 stars beyond. In the UV grism, the spectra of the *F*0 stars suffer contamination from order overlap for $\lambda > 5000$ Å. The correction for coincidence loss was applied to all spectra.

Table 5. Flux calibration sources with low coincidence loss used for the initial effective area determination at the default position. See also Table 2.

Grism mode	Source name	Number of spectra	Coincidence loss
UV nominal	WD1657+343	8	≤5 per cent
UV nominal	WD0320-539	8	≤9 per cent
UV nominal	WD1057+719	7	≤9 per cent
UV nominal	GSPC P177-D	14	≤5 per cent
UV nominal	G63-26	3	≤10 per cent
UV clocked	WD1657+343	4	≤5 per cent
UV clocked	WD0320-539	7	≤9 per cent
UV clocked	WD1057+719	8	≤9 per cent
UV clocked	GSPC P177-D	2	≤5 per cent
UV clocked	GSPC P 41-C	2	≤7 per cent
UV clocked	G63-26	2	≤10 per cent
Visible nominal	WD1657+343	2	≤10 per cent
Visible nominal	GSPC P177-D	1	≤10 per cent
Visible clocked	WD1657+343	1	≤13 per cent
Visible clocked	GSPC P177-D	1	≤14 per cent

Initially, the effective areas were derived for the faintest sources at the default (centre) positions primarily to minimize the effects of coincidence loss. The faintest sources, WD1657+343, and WD1121+145, have count rates less than or comparable to the background. GSPC P177-D, GSPC P 41-C, WD0320-539, are only slightly brighter, so their coi-correction is still considered small in the UV grism but is unfortunately larger in the visible grism, see Table 5.

Many calibration spectra used here were taken early in the mission, especially for the visible grism, and so do not have a corresponding image in one of the lenticular filters taken right before or after the spectrum. For those, if possible, the accuracy of the wavelength scale was corrected prior to the derivation of the effective area using the spectral features. Without doing this correction, dividing by the reference spectrum $F_{\rm cal}$ caused large excursions in the effective area near spectral lines.

Finally, the effective areas derived from individual spectra and from each source were summed, weighted by the error on the data. The resulting effective areas were fit by a smoothing spline to remove noise. The brighter sources were included next, and it was confirmed that they gave an effective area consistent with that of the weak sources alone, but with a smaller effective area error. The resulting effective areas are shown in Fig. 22.

The accuracy varies by location on the detector and by detector mode, and the available total exposure in the calibration spectra, see Table 6. The smaller effective area at shorter and longer wavelengths means the errors in $A_{\rm eff}$ grow larger as a percentage of the values.

Note that at the default positions the effective areas for the nominal and clocked grism modes for each grism are nearly identical, as would be expected since they are formed by the same optical elements.

Downloaded from http://mnras.oxfordjournals.org/ at NASA Goddard Space Flight Ctr on November 17, 2015

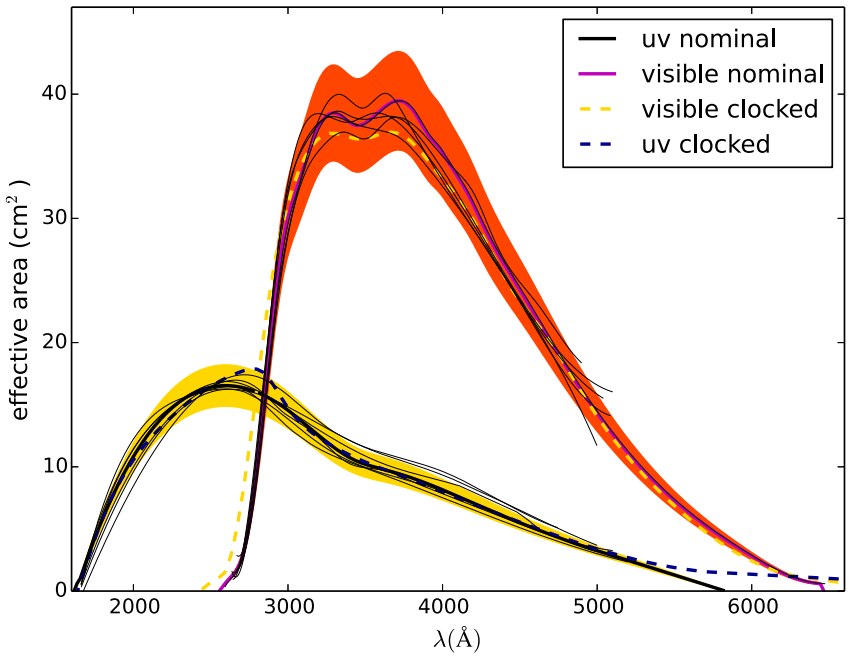

Figure 22. The effective areas for the nominal mode. Shaded areas show the 1σ errors. Thin lines show the samples of the effective area from different locations on the detector. The dashed curves show the clocked grism effective areas at the default position for comparison.

8.2 The effective area over the whole detector

It is useful to first consider the model predictions for the variation of the throughput over the detector. For a spectrum at an offset position, the model can be used to predict the ratio of the effective area to that on-axis.

For the nominal mode of each grism, the throughput is predicted to vary slowly, typically by less than 5 per cent from the on-axis value over the detector. However, for the clocked grism modes the throughput varies much more. Fig. 23 shows the results for the UV grism. Positions were varied for fixed X and fixed Y anchor position to illustrate this variation.

For the effective area determination over the whole detector all sources, including those with a larger coincidence loss were used, after making the coincidence loss correction described in Section 7.1.

The locations on the detector where calibration spectra were taken are shown in Fig. 24, with one panel for each grism mode. Notice that the UV grism clocked mode includes a fair number of observations in the upper right hand corner, where the second order is shifted away from the first order, allowing the use of the first order up to 4500 Å. Additional observations were made in the upper left corner, where the sensitivity is found to drop off in the clocked modes. Also, there are proportionally more spectra from a larger variety of calibration sources taken near the default position. For each grism mode, about 100 spectra from a range of sources were available for the calibration.

The positioning of the early calibration spectra did not use a 'slew-in-place',[15] and therefore were not always found at the intended positions.

Spectra that are near to each other and contain both blue and red spectra can be grouped to give an effective area. We find that the variation of the effective area as measured at different positions for the nominal grism modes is consistent with the model predictions within the uncertainties. For that reason, we have decided to treat the effective areas for the nominal grism modes to be constant over the detector within the quoted error.

Based on differences between blue (WD) and redder (F0) calibration sources, possible contamination due to the second-order contribution increase from 20 per cent up to 80 per cent between 5000 and 6600 Å in the visible grism nominal mode.

For the clocked grism modes, the variation of the effective area over the detector is predicted to be smoothly varying. However, the observed effective areas in some locations were noisy due to limited data. To remove this noise, the ratio of the effective area to that at the default position was constrained to be a smooth polynomial fit. The resulting effective area varies smoothly over the detector.

In Fig. 25, for the clocked modes, effective areas are shown for locations where sufficient observations were available. The position of the effective area on the detector is indicated by the anchor position given in the legend. At a glance, one can see that in the clocked grism modes the effective areas for anchor positions with small X-coordinate are markedly smaller, and have a cut-off at some wavelength towards the red. The variation in sensitivity and the cut-off at long wavelengths for the left-hand side of the detector was qualitatively confirmed by the model for the clocked grism.

It is useful to make a comparison to the effective area of the UVOT *white filter* (see Fig. 28) which is transparent. The visible grism effective areas for the wavelengths above 3000 Å are smaller and fall off just like in the *white filter* (Poole et al. 2008); also the bumps at the peak correspond in wavelength to those seen between 3000 and 4000 Å in the *white filter*.

8.3 The accuracy of the effective area calibration

In Table 6, the errors from the determination of the effective area have been listed. The error due to the accuracy of the calibration

[15] A slew in place means the spacecraft is commanded to do a second positioning refinement which enables the accurate positioning of the spectrum on the detector to within about 20 pixels.

Downloaded from http://mnras.oxfordjournals.org/ at NASA Goddard Space Flight Ctr on November 17, 2015

Table 6. Typical errors in the effective area.

UV grism	Anchor	Per cent error at 1750 Å	Per cent error (1,3)	Per cent error (2,3)	Notes
Nominal	[1000,1080]	30	15	15	(4)
Clocked	[1140,1030]	19	9	9	(5)
Clocked	[1160, 585]	12	6	9	
Clocked	[1240,1300]	9	6	9	
Clocked	[1530, 730]	11	6	9	
Clocked	[1545,1300]	9	7	9	
Clocked	[1610,1575]	18	9	9	
Clocked	[1820,1700]	28	5	9	
Clocked	[595,1285]	20	9	9	
Clocked	[735,1260]	20	9	9	
Clocked	[785, 695]	6	7	9	
Clocked	[880,1550]	13	7	9	
Clocked	[980,1405]	20	9	9	
Visible grism	Anchor	Per cent error at 6000 Å	Per cent error (1,3)	Per cent error (2,3)	notes
Nominal	[1050,1100]	13	11	11	(4)
Clocked	[1141,1030]	11	15	15	(5)
Clocked	[1630,1130]	11	9	15	
Clocked	[1270, 600]	11	9	15	
Clocked	[1300,1485]	11	7	15	
Clocked	[1410,1410]	11	10	15	
Clocked	[1105,1445]	11	10	15	
Clocked	[1610, 985]	11	9	15	
Clocked	[765, 960]	11	6	15	
Clocked	[880,1410]	11	10	15	
Clocked	[800,1200]	11	15	15	
Clocked	[990, 600]	14	6	15	
Clocked	[590, 640]	30	13	15	

Notes. (1) rms error from consolidated EA for each source.
(2) Recommended error.
(3) Errors based on where $A_{\rm eff}$ is larger than half the maximal value. They will be larger at wavelengths with lower effective area. Typically that applies to the ranges 1950–4400 Å(UV) 2850-4800 Å(visible).
(4) Effective area at ±600 pixels from the default position.
(5) Effective area at ±80 pixels default position.

spectrum, and the Poissonian noise in the spectrum and background is typically 3–4 per cent after averaging over about 5–10 spectra, and has not been listed for each effective area result. The combined rms error derived for each wavelength from the effective area from all relevant spectra combined is listed in the third and fourth columns. The third column lists the value at a fixed wavelength outside the mid-sensitivity range, while the fourth column lists the maximum value at the middle of the sensitivity range. For the UV grism, the sensitivity is already quite low at 1750 Å and this wavelength has been given specifically to give a measure of the largest error expected in the blue part of the UV range where the sensitivity gets low. For the visible grism, the sensitivity at the short wavelengths drops off so rapidly, that the error given for the range in column 5 is often that at around 2850 Å, where the effective area is about half the peak value. The value at 6000 Å has been chosen since the spectrum at longer wavelengths has a low effective area. For all effective areas, the errors reach a minimum value of around 5–8 per cent near the peak effective area.

To understand the effect of the error introduced by coincidence loss in our effective area determination, we considered the following. The error in the coincidence loss is proportional to the error in the count rates shown in Figs 16, 17, 18 and 19, so typically a 5–10 per cent error is introduced. The magnitude of the coincidence loss correction depends on the calibration source used, and so does its error. For sources less bright than the background, the accuracy of the background determination is a source of error. The background changes when the roll angle of an observation varies due to unresolved zeroth orders and is difficult to measure. However, the error is unlikely to exceed 10 per cent or the observed variation in count rates for weak sources would be larger. The other factors contributing to the error in the effective area are the random measurement errors and the uncertainties in the flux standards. At some detector locations, only a very limited number of calibration observations were available to derive the effective area and variance between the observations is found to be lower than in areas with many spectra from different sources. In that case, there is no proper sampling of the variance in the measurements.

Finally, considering all these effects, in the fifth column the recommended uncertainty in the effective area is listed. For the nominal grism effective areas, which were determined at various offsets, the accuracy was such that these were deemed consistent with the effective area at the default position.

The effective area curves in the UV grism above 4900 Å may have been affected by some second- and third-order emission, which tends to increase the resulting effective area. This contaminating emission is present above 5000 Å in the F0V spectra that were

Downloaded from http://mnras.oxfordjournals.org/ at NASA Goddard Space Flight Ctr on November 17, 2015

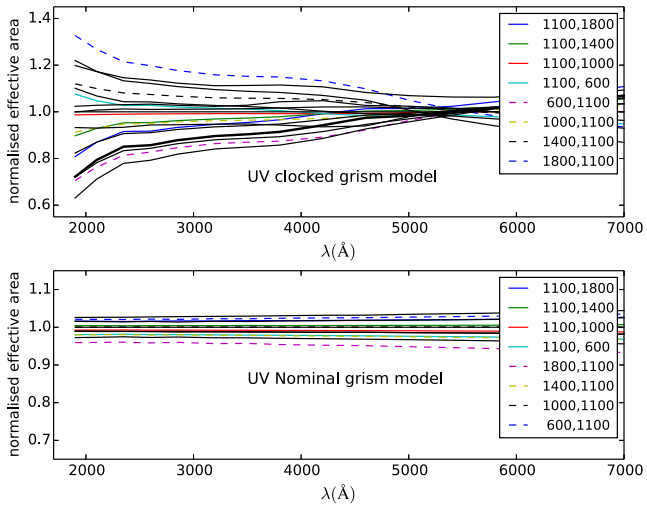

Figure 23. The variation of the normalized effective area as predicted by the model for spectra with anchors at various locations on the detector. Effective areas are plotted for the set of anchor positions with X=1100,Y varying and Y=1100, X varying, to illustrate the variation for the clocked (upper) and nominal (lower) grisms.

used. This would be especially so for the effective areas with order overlap, but not for those in the UV grism clocked mode at the large offset at high anchor (X,Y) coordinates. The effective areas all show a similar slope, so that the effect is thought to be less than 20 per cent above 5000 Å. In the visible grism, the second order is much weaker since the grism was blazed. The only indication of second-order contamination is that the flux in WDs shows some enhancement above 4900 Å. For the effective area above 4900 Å, only P177D and P041C of spectral type F0 were used which are not expected to have second-order contamination in the visible grism.

8.4 Effective area for the second order

There are two ways in which the second-order count rate can be measured and separated from the first-order count rate.

The first method is where orders completely overlap, and given an accurate effective area for the first order, the second-order contribution can in principle be found by subtraction. The correction for coincidence loss treats the total flux of first and second order combined, and this has to be used appropriately in the analysis. The second method is at a large offset position in the UV grism clocked mode . There the second-order separation from the first order allows us to measure the count rate of that separated part of the second order. Here also a good wavelength calibration for the second order is

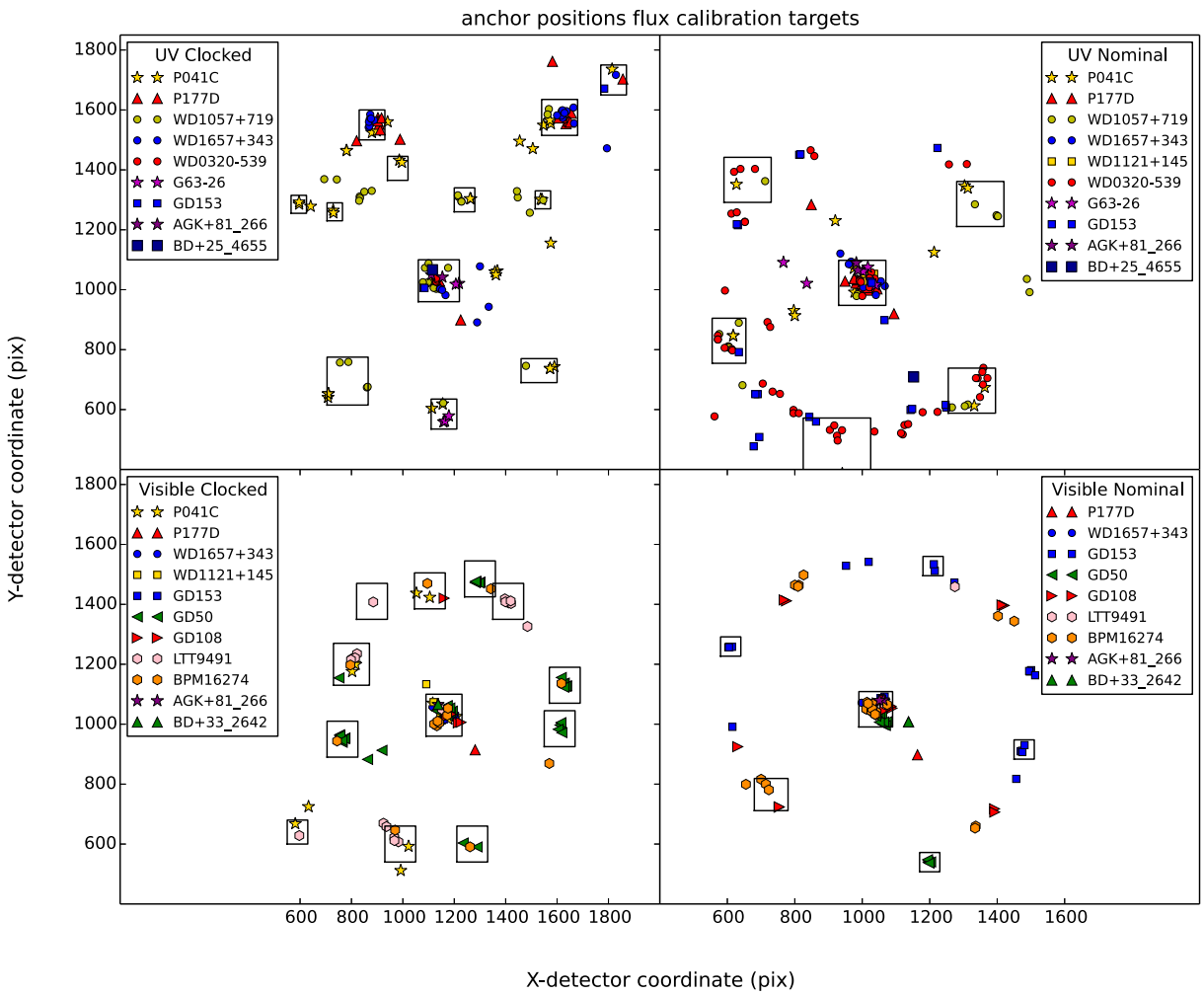

Figure 24. The location of the anchors for all the flux calibration spectra. The boxes indicate spectra which have been averaged together for that position.

Downloaded from http://mnras.oxfordjournals.org/ at NASA Goddard Space Flight Ctr on November 17, 2015

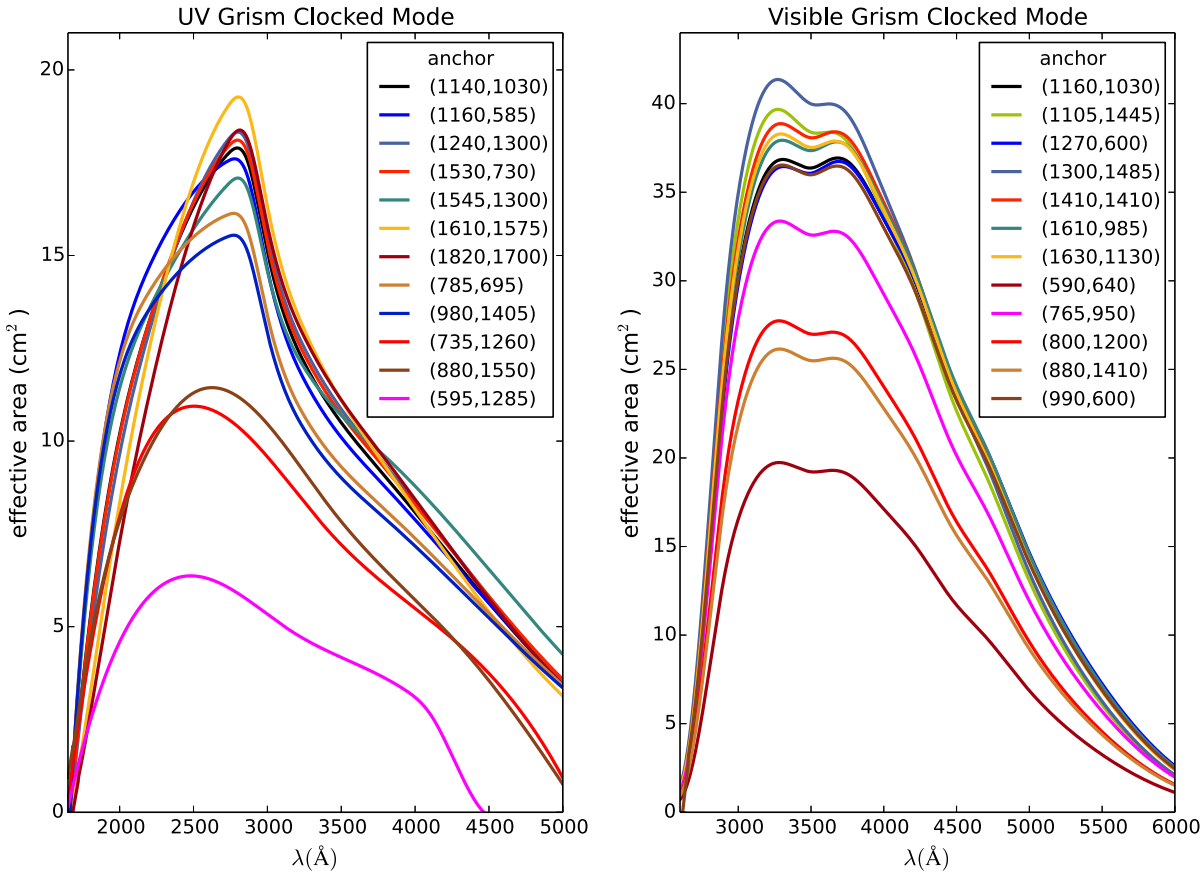

Figure 25. The effective areas for the clocked modes at various offsets. The offset is labelled according to the anchor position in detector coordinates.

needed. The noise in the measurement requires a reasonably bright source. However, the source cannot be too bright since then the first order will affect the second order by coincidence loss. We will only consider the first method here.

To derive the second-order effective area at the default position, we used the observed rates after subtracting the background, and applying the coincidence loss correction. The rate due to the first order was then derived using the reference spectrum and the known first-order effective area. This rate was subtracted to obtain the second-order rates, already corrected for coincidence loss. The second-order rates were subsequently used in equation (6) to derive the second-order effective area, limited to the default cross-dispersion width of the first order. This is the most useful measure of the size of the second-order contamination affecting the first order.

We examined the results for the various flux calibration sources, and found that GD153 and WD1057+719 gave results which were consistent with the much noisier data from the other sources.

The error in the second order is rather large, as it includes a subtraction of the first-order effective area, and the noise is also larger for that reason. For the error on the first-order effective area a conservative 11 per cent was adopted. The error on the second-order effective area for an individual spectrum then ranges from 20 to 40 per cent. The derived effective areas were averaged over multiple spectra which reduces the error to that shown in Fig. 26.

In the UV grism clocked mode, the second order becomes displaced normal to the dispersion direction with the size of displacement dependent on position of the spectrum on the detector. In these cases, a different part of the second order will contribute to the first order. Estimating the effective area of the second order to compute

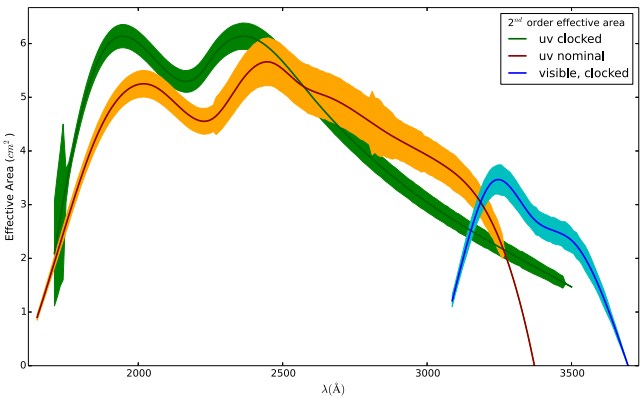

Figure 26. The effective areas of the second order in the UV grism and visible grism at the default position. The effective area is shown as function of the second-order wavelength. Shaded regions indicated the uncertainty in the effective area of the second order.

the contamination in the first order is thus only providing an approximate upper limit for spectra away from the default centre position. In the visible grism, the orders overlap over the whole detector and this issue does not occur.

Comparison to the first-order effective area in Fig. 22 shows that the second-order effective area in the UV grism is less than half that in the first order for equivalent wavelength, but in the visible grism, the second-order effective area is less than 10 per cent of that in the first order which means that usually it can be disregarded except where the first-order effective area is very small, i.e. at long

Downloaded from http://mnras.oxfordjournals.org/ at NASA Goddard Space Flight Ctr on November 17, 2015

wavelengths. In the UV grism, the first-order effective area at long wavelengths is overtaken by the second-order effective area, resulting in equivalent effective areas on the detector at around 4800 Å in first order and at 2600 Å in the second order, after which the second-order effective area is larger than that of the first order.

9 THE ZEROTH ORDER IN THE UV GRISM NOMINAL MODE

9.1 Zeroth-order effective area

The zeroth-order dispersion as predicted by the model can be fit approximately by a rational function as

$$\lambda = 1220. - 110715/(p - 35.6) \quad \text{Å}, \tag{7}$$

where p is the pixel distance to the anchor point. The anchor point of the zeroth order is not directly measurable, but is selected to be close to the peak of the zeroth-order emission.

As we show later, the zeroth order in the UV grism provides a similar response to the b-band filter.

The dispersion relation can be used to predict the wavelengths that fall on a pixel. When doing that, it is clear that at the longer wavelengths a large part of the spectrum falls on only a few pixels, while the UV part of the spectrum is spread out into a relatively large tail. Of course, the peak emission will be spread out over several pixels, since the instrumental PSF is about 5 pixels FWHM for the zeroth order.

The calibration spectrum was compared to the measured zeroth-order counts. Since the red part of the spectrum falls on such a few pixels, a faint white dwarf spectrum is ideal for calibrating the zeroth order since its flux rises in the blue and is faint, so that coincidence loss is very minor.

The natural way to proceed is to convert the CALSPEC WD 1657+343 spectrum $F_{\rm cal}(\lambda)$ as a function of wavelength to a count rate spectrum as a function of pixel distance to the anchor point, which we define as $C_{\rm cal}(p)$, with the anchor point chosen appropriately.

$$C_{\rm cal}(p) = \int_{\lambda 1}^{\lambda 2} F(\lambda)(\lambda/hc)\mathrm{d}\lambda, \tag{8}$$

where $\lambda 1$ and $\lambda 2$ are bounding wavelengths of the pixel p. The spectrum is then converted to count rate by dividing the flux by the photon energy.

In Fig. 27, the calibration reference spectrum of WD1657+343 is shown as it should appear in zeroth order. Although the flux rises to the blue, the predicted counts per bin peak in the red near 4350 Å due to the nonlinear dispersion. The wavelength range inside a single bin increases so much towards the red part of the spectrum that it leads to a counter-intuitive WD flux(bin) spectrum for those of us who are used to the normal flux rising in the blue in a flux(wavelength) plot. With the non-linear dispersion of equation (7), the anchor at p=0 corresponds to $\lambda = 4329$ Å, which is the b-band effective wavelength. 10 bins up, at $p = +10$, the median wavelength of the v filter is passed, while at $p = +25$, the wavelength is more than 7000 Å, at which point the effective area of the instrument will cut off any further contribution.

With the effective area definition based on the counts per pixel using equation (8), the expression for the effective area simplifies to

$$A_{\rm eff}(p) = C_{\rm obs}(p)/C_{\rm cal}(p), \tag{9}$$

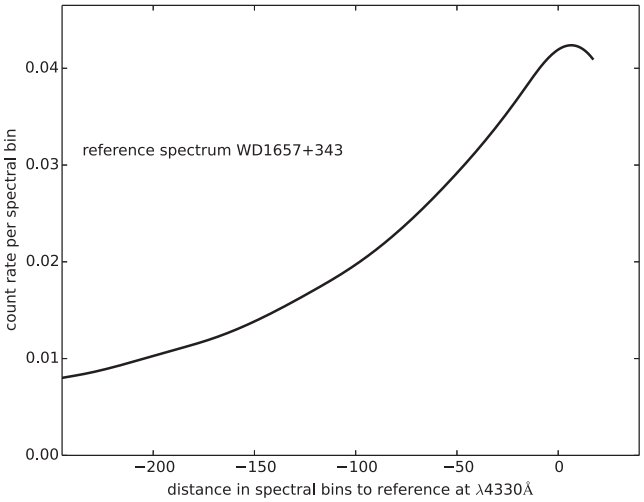

Figure 27. The white dwarf reference spectrum of WD1657+343 converted to counts per spectral bin per cm^2 for the adopted zeroth-order dispersion. The size of the spectral bins increases hyperbolically with wavelength. This shifts the peak to the red.

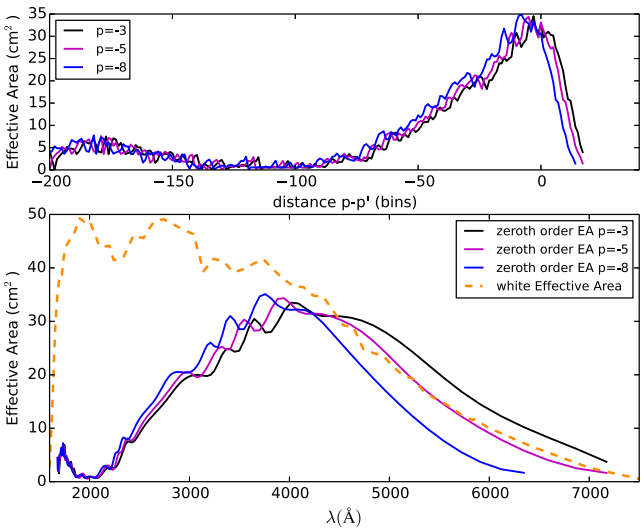

Figure 28. The effective area for three values of $p - p'$. The top panel shows how the effective area is distributed in the observed spectrum, while the bottom panel shows the smoothed effective area as function of wavelength. Note that in the UV there is a small response. The effective area of the white filter should be larger than that for the grism zeroth order.

with $C_{\rm obs}(p)$ the observed count rate per pixel,[16] and $C_{\rm cal}$ is the count rate per pixel per cm^2, see equation (8). The measurement is really $C_{\rm obs}(p')$ with $p' \neq p$, since we do not know where in the spectrum the anchor point really lies, resulting in an uncertainty in matching the calibration spectrum to the observed spectrum. However, we are aided by the small number of pixels that the red part of the spectrum falls on, and also that the effective area drops to zero far short of the longer wavelengths covered by the grism if the anchor in the spectrum is made to be at too short a wavelength. Furthermore, as another check, the white filter, which is blank, should have a larger effective area than the grism (see Fig. 28).

[16] Coincidence loss is present but neglected here.

Downloaded from http://mnras.oxfordjournals.org/ at NASA Goddard Space Flight Ctr on November 17, 2015

To study the sensitivity of the result for other choices of $p - p'$, several other cases were computed. For our preferred choice, the peak in the observed count rate spectrum was matched to the adopted anchor point in the calibration spectrum to derive the effective area. Then, an offset of several pixels to either side was applied and the effective area was rederived. A smoothing spline was applied to remove the noise. The result shown in Fig. 28 gives the effective area for three offsets. The reddest peaking curve actually has too large an effective area when comparing with that of the *white* filter effective area. Therefore, we exclude the reddest peak from further consideration. The next offset p=−5 peaks at 3920 Å, and closely matches on the red side the effective area of the *white* filter. The p=−8 is perhaps the best match with the effective area below that of the *white* filter, with a peak at 3740 Å, while also the shape conforms better to the *white* filter. The UVOT *u* filter has a central wavelength of 3465 Å, while for the *b* filter it is 4392 Å. With the unknown effects of the coincidence loss in the zeroth order its effective area is considered to be compatible with either the *u*- or the *b*-band filter. In the next section, this has been investigated further.

The visible grism has a much weaker zeroth order. Applying the same analysis as for the UV grism, we find a peak at 4200 ± 200 Å with a peak effective area of 6.6 cm^2.

9.2 Photometry with the zeroth order in the UV grism

The zeroth orders are still present with reasonable signal to noise even when the first order is too faint to distinguish from the background. With the UV grism nominal mode in the automated response sequence typically taking an exposure 300–350 s into a GRB, we can still use the zeroth orders for the fainter bursts to obtain an equivalent magnitude.

As we have seen, the zeroth-order emission is extended. Sources with different spectra and thus different spectral energy distributions will tend to peak slightly differently in the zeroth order. However, as we have seen in Fig. 27, even from a very blue source the redder photons are those most readily detected in the zeroth order.

In our method, the adopted approach is to put an aperture which is a 10 arcsec (about 20 pixel) radius circle at the location of the zeroth order in the grism detector image using the WCS-S sky position after a successful application of UVOTGRASPCORR.

For the photometric calibration, the same calibration sources as in Poole et al. (2008) were used.

The measured count rate was compared to the photometry in *v*, *b*, and *u*, and showed that the photometry is most closely matched to that in *b*, which has an effective filter wavelength of 4329 Å. Red stars with $u - v < 2$ or $u - b < 1.1$ were excluded. The best-fitting zero-point is 19.46 for a UVOT *b* magnitude on the Vega system. The two panels in Fig. 29 show the UV grism magnitude as determined by using this zero-point versus *b* magnitudes and the residuals. The three panels in Fig. 30 show the residuals against colour.

We found a significant dependence of the grism – *v* magnitude on colour, but not so strong with grism – *b* magnitudes, and for that reason we derive an equivalent *b* magnitude from the grism zeroth order. For a source which is not redder than $u - v = 2$ or $u - b = 1.1$ then the count rate in a 10 arcsec circular aperture in the UV grism can be used to determine the *b* magnitude with an error of 0.23 mag rms.

For verification of the validity for GRBs, the data from GRB081203A (Kuin et al. 2008) and GRB081222A were used. The GRB magnitudes and colours were derived from their spectra and lightcurves. The grism magnitude and error were derived as

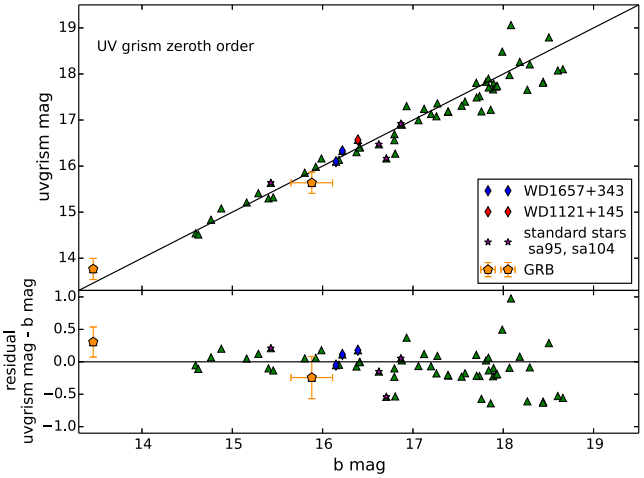

Figure 29. The UV grism zero-point magnitude derived using zp=19.46, compared to UVOT *b*. The GRB data have only been used for verification.

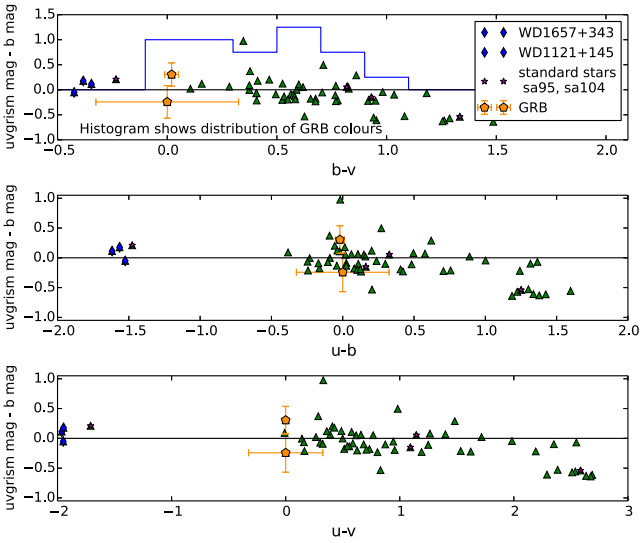

Figure 30. The UV grism zero-point colour dependence residuals. The GRB data have only been used for verification.

described above and they were plotted in Figs 29 and 30. It can be seen that the GRB grism magnitudes are consistent with the calibration.

10 THE GRISM UVOTPY SOFTWARE AND OUTPUT FILE FORMATS

This calibration has been incorporated into a software package written in the PYTHON language. The basic parts of the software were originally written to perform the calibration and were converted into a tool for users. The UVOTPY software (Kuin 2014) was released in several steps while the calibration was ongoing, and includes at present the latest calibration files. It requires the normal *Swift* UVOT software and CALDB which are used for example for further processing the data. The code also depends on several other PYTHON packages, like MATPLOTLIB.[17] The software can be downloaded from the UCL/MSSL UVOT website.[18]

[17] http://matplotlib.org
[18] See http://www.mssl.ucl.ac.uk/www_astro/uvot/

Downloaded from http://mnras.oxfordjournals.org/ at NASA Goddard Space Flight Ctr on November 17, 2015

The UVOTPY software writes the extracted spectral data to FITS format files. The main file has several extensions. The first extension contains the data for use with the XSPEC[19] program, though the redistribution matrix file is only produced when a parameter is set in the call. The rates have been corrected for coincidence loss. The second extension is of interest to non-XSPEC users and contains in a binary table columns, for the first order: the wavelength, the net count rate and background count rate uncorrected for coincidence loss, the coi-corrected flux, the coi-correction factor that has been applied, the channel number, and the aperture correction factor which was applied in the calculation of the flux. Optionally, the second-order wavelength, count rate, and background are supplied, and the rates in the coincidence area. A flag column lists the automatically generated flags. These provide warnings of, for example, possible nearby zeroth orders.

Spectral extraction requires at a minimum the sky position in RA and Dec. in decimal degrees, the observation ID, and the grism detector file extension with the spectrum to be processed. Optional parameters control such things as the data directory path, whether the second order should be extracted separately (for offset observations where the orders split), and the background region(s) for the spectrum.

The program automatically derives the anchor position by using information in the (optional) lenticular filter image header(s), the grism detector image file header, and calibration files. Based on the anchor location the curvature of the spectrum is found, and the angle under which the spectrum lies on the detector image. A slice around the spectrum is extracted and rotated which involves a resampling. The rotated image slice is then used to extract the spectrum. The count rate within the spectral track is extracted. The first and second order are extracted independently, so where there is overlap, the counts end up in both first and second orders. A plot is made to show the extracted count rates of the first and second orders, and the first-order count rate spectrum is used to make a prediction of the second-order count rate. Comparison of the first and second orders based on pixel position can help determine the location of second-order features in the first order. The program makes a flux calibration by applying the coincidence loss correction and effective area, and writes the results to the output files. A plot shows the flux calibrated spectrum, and a very rough estimate of the second-order spectrum, if present.

Since the width varies slightly from exposure to exposure, to ensure the same encircled energy in an extraction, the spectra are extracted after fitting the width of the spectral track with a Gaussian curve, interpolating the result with a polynomial to remove the effect of MOD-8 noise on σ and using a width of 2.5 σ.

In more detail, the following steps are used to extract the spectra.

(i) The anchor position is determined.

(ii) The image is rotated around the anchor using the model dispersion angle for the anchor. After the rotation, the zeroth order and UV part of the spectrum is to the left, the higher orders and longer wavelengths to the right. Due to the curvature, the spectrum is generally not completely aligned with the *x*-axis.

(iii) The rotated image is clipped 100 pixels above and below the centre.

(iv) The curvature of the spectrum is retrieved.

(v) A correction is made for the distance of the anchor to the centre of the spectral track.

(vi) A Gaussian is fit to the width of the spectral track over 30 pixel slices along the dispersion and interpolated with a polynomial.

(vii) The counts are extracted in a curved slit (default halfwidth 2.5σ).

(viii) The aperture correction is computed.

(ix) The flags are populated based on catalogue sources near or on the spectrum.

(x) The slit parameters are saved.

(xi) The coincidence loss factor is calculated and used.

(xii) The background counts are subtracted.

(xiii) Statistics are calculated.

The background calculation is performed as follows.

(i) An initial background image is made from the rotated image.

(ii) Pixels $>3\sigma$ above the mean, are replaced with the mean of the 3σ clipped image.

(iii) The background image is divided into 80 areas in the dispersion direction (where the background varies in the clocked image).

(iv) For each area bright pixels, where (data $>mean + 2\sigma$), are replaced with the mean.

(v) The spectrum is smoothed using a boxcar filter 50 pixels along dispersion, 7 pixels across dispersion direction.

(vi) The background is extracted from default regions or as requested.

(vii) The background regions are interpolated to match the extraction slit of the spectrum.

The result is a robust background estimate. In very crowded fields, the background may include unresolved spectra, while excluding the stronger spectra present. Zeroth orders are properly masked out as well.

Flags are maintained for bad or possibly bad areas. The `uvotgetspec.quality_flags()` defined values are: 'good': 0, 'bad': 1, which means the data is definitely bad; 'zeroth':2, which means there is a zeroth order near the spectrum 'weak zeroth': 4, which means that the zeroth order near the spectrum does not have a halo; 'first': 8, there is contamination by a first-order spectrum; 'overlap': 16, which means another spectrum overlaps the target spectrum.

Although it was hoped we would be able to separate out the different orders in an iterative way, that has not proved possible. The coincidence loss complicates matters where different orders affect the result.

11 HOW AND WHEN TO USE THE GRISMS

11.1 Determining if a source can be observed in the UVOT grism

With a complicated interplay between effective area, coincidence loss in both background and spectrum, and incident flux, some guidance is needed for determining when the UVOT grisms are likely to return a useful spectrum.

For faint spectra, the level of the background determines the signal to noise. Backgrounds can vary during the orbit, for example due to Earth shine, and depend also on the sky background, mainly the zodiacal light, which depends on the distance to the ecliptic. Some details were provided in Breeveld et al. (2010). The *Swift* orbit of 90 min limits the length of a single observation. Multiple exposures can be added together to improve the signal to noise of a weak spectrum. For example, during the fading of SN2010aw

[19] http://xspec.gsfc.nasa.gov

Downloaded from http://mnras.oxfordjournals.org/ at NASA Goddard Space Flight Ctr on November 17, 2015

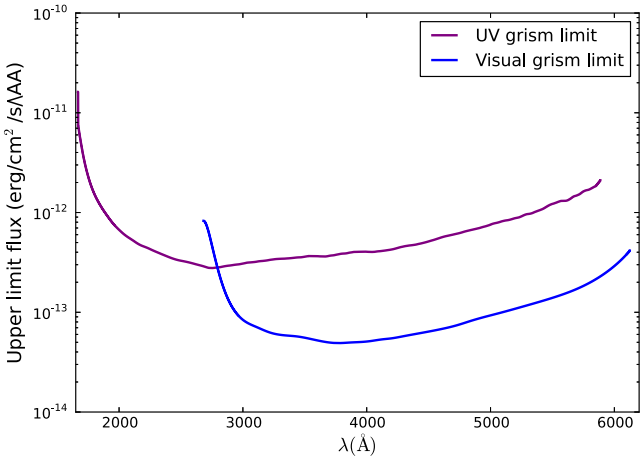

Figure 31. The largest incident flux that the UVOT grisms can observe and that can be corrected for coincidence is shown for each detector. Larger fluxes are not calibrated, or may damage the detector.

(Bayless et al. 2013), the last spectrum was obtained from summing nearly 20ks of exposure. The spectra from individual exposures can be extracted and summed with appropriate weights, or alternatively, the images can be aligned on the anchor points and summed. The success of the latter method depends on the accuracy of the anchor positions, and usually requires the same roll angle so that zeroth orders of field stars align as well. For the analysis in this paper the first method was used throughout.

For bright sources, especially variable ones, it is difficult to give a limiting brightness. The limit is reached when the effects of coincidence can no longer be corrected. From equation (3) the determining factor for the size of the coincidence is the incident count rate per frame. An inspection of the flux for the bright WD GD153 in the UV grism around 2700 Å, that is at the peak of the effective area, shows the flux to be around 1.3×10^{-13} ergs cm^{-2} s^{-1} Å^{-1} (see Fig. 20). The coincidence loss factor there is $F_{\rm coi} = 1.30$. In the visible grism, the coincidence loss for GD153 peaks even higher, at a factor $F_{\rm coi} = 1.70$, but there the continuum spectrum starts to be affected rather severely by the coincidence loss.

Assuming an intermediate value as a reasonable limit for the coincidence loss of $F_{\rm coi}^{\rm limit} = 1.5$, the corresponding incident count rate per bin per frame is 2.2. Using equation (6) the following inequality follows:

$$F_{\rm cal} < \frac{2.2h\nu}{A_{\rm eff} \times (\Delta\text{Å/bin})} \text{erg cm}^{-2}s^{-1}\text{Å}^{-1}, \quad (10)$$

with $h\nu$ the photon energy in erg. For the UV and visible grism, we can thus graphically plot the upper limits using the typical effective areas and dispersion, and it is shown in Fig. 31. The approximations made mean the upper limit is given to within about 30 per cent. If an observation is available for a lenticular filter, that can be used to judge whether the part of the spectrum covered by the band is observable, see Table 7. For example, if the magnitudes in the UV filter are below the limit, but the *u*,*b*,*v* filters are above the limit, the part of the spectrum above 3000 Å is likely to be overexposed.

11.2 Using a smaller aperture

It is sometimes advantageous to extract the spectrum with a smaller extraction width. To convert the measured count rates requires that the aperture correction is known for the photons missed because they fell outside the extraction area.

Table 7. Bright upper grism limit judged by photometric UVOT (Vega) magnitude.

Filter	Range[4]	UV grism	Visible grism
v	5010–5880	8.78	11.07
b	3775–4930	10.28	12.54
u[3]	3000–3080	9.99	12.00
*uvw*1	1720–3130	10.09	(1)
*uvm*2	1909–2650	9.96	(2)
*uvw*2	1610–2850	9.32	(2)
white	1650–7300	9.84	

Notes. (1) Only a small overlap to the sensitive range of the visible grism makes this band not useful.
(2) No overlap with the visible grism.
(3) Red leak at 4750.
(4) Range with effective area larger than about 2 cm^2.

The profile across the spectral track is mainly determined by the grism optics but in a small number of observations the width of the spectrum is larger than the usual width, perhaps because the spacecraft pointing drifted more than could be compensated for by the shift-and-add algorithm. For that reason, the aperture correction is scaled to the sigma of a fitted Gaussian of the profile across the dispersion direction. This ensures that the energy contained within a certain aperture is insensitive to the small changes of the width of the spectral track. The measured encircled energy (see Fig. 6) is used to do an aperture correction to the observed count rate. The coincidence loss correction is then computed as before, but after the aperture correction has been done.[20]

Coincidence loss also causes a MOD-8 pattern, and as a result the aperture correction becomes inaccurate for the brighter sources. It is therefore recommended to check the results also by using the default aperture.

11.3 Some tips for using the grism data

Very rarely a data dropout causes a line of data in the image to be lost. Since this used to cause the UVOTPY software to crash, the data are now automatically replaced with the average of the next lines. The flagging does not keep track of that at the present time, so only inspection of the image can show it. A data dropout can appear to be an absorption line in a spectrum if it is not corrected/replaced.

The UVOT images all show a column where a few pixels are wrapped from the right-hand side of the image to the left-hand side. This can cause a few very bright pixels at the end of the spectrum, especially in the clocked modes. To some extent the software ignores this in, for example, determining the background, but in rare occasions that may show up as a problem.

If the field as a whole has a high count rate, the UVOT data processing cannot handle all the data coming from the CCD within one frame time. That means that the upper part of the image does not get stored and appears black. There is then a small region between the image at the bottom and the dark top where the count rate ramps up. This is thought to be governed by the statistical fluctuations in the incoming rate. It seems that the bottom part of such an image is correctly exposed, and tests on both photometry and spectra support this.

[20] Due to a software bug, the aperture correction did not work correctly for UVOTPY software version 1.0. It has been corrected since.

Downloaded from http://mnras.oxfordjournals.org/ at NASA Goddard Space Flight Ctr on November 17, 2015

Most recent grism exposures are taken in a mode which pairs them with a lenticular filter. The spectra can then be extracted by either using the lenticular filter image to refine the astrometry or using the header information after a correction with UVOTGRASPCORR which routinely is applied during ground processing. The larger wavelength errors when using UVOTGRASPCORR are disappointing, since early in the mission many grism exposures were taken without a lenticular filter exposure. Further work may be able to overcome this limitation so that better wavelengths can be obtained for all UVOT spectra.

Since the wavelengths are determined from the distance in pixels to the anchor, an erroneous anchor position can lead to a distortion in the wavelength scale of tens of angstroms at the end of the wavelength range. If the anchor position shift is known, this can be corrected by rederiving the wavelengths using the dispersion relation for the spectrum given in the header.

ACKNOWLEDGEMENTS

Throughout the calibration many people provided feedback and helped refine the understanding of what was possible and what could be improved through their use of the grisms for observational studies. We wish to thank all of them for their efforts, help and patience. A special thanks goes to all the Swift planners who through their effort ensured the success of this calibration. The optical design of the grisms was by the late Richard Bingham. We are grateful to Fred Walter, Ed Sion, and Greg Schwartz for sharing their *HST* and optical spectra, some of which were taken during several Swift-*HST* observing campaigns, which helped the calibration effort. This work was supported by the UK Space Agency through a grant for *Swift* Post Launch Support at UCL-MSSL. This work is sponsored at PSU by NASA contract NAS5-00136. We acknowledge the use of data from the SIMBAD and Vizier data bases at the CDS in Strassbourg, the online WR spectra from Hamann, the STScI MAST and HLA archive, the ESA INES *IUE* archive, the HEASARC archives, and the NIST atomic data base on the WWW. We used 'Astropy', a community-developed core PYTHON package for Astronomy (Astropy Collaboration, 2013).

REFERENCES

Astropy Collaboration , 2013, A&A, 558, 33
Barthelmy S. et al., 2005, Space Sci. Rev., 120, 143
Bayless A. J. et al., 2013, ApJ, 764, L13
Bodewits D., Villanueva G. L., Mumma M. J., Landsman W. B., Carter J. A., Read A. M., 2011, AJ, 141, 12
Boggess A. et al., 1978, Nature, 275, 372
Breeveld A. et al., 2010, MNRAS, 406, 1687
Breeveld A., Landsman W., Holland S. T., Roming P., Kuin N. P. M., Page M. J., 2011, AIP Conf. Proc, Vol. 1358, Gamma Ray Bursts 2010. Am. Inst. Phys., New York, p. 373
Brown P. et al., 2012, ApJ, 753, 22
Bufano F. et al., 2009, ApJ, 700, 1456
Burrows D. et al., 2005, Space Sci. Rev., 120, 165
Byckling K., Osborne J. P., Wheatley P. J., Wynn G. A., Beardmore A., Braito V., Mukai K., West R. G., 2009, MNRAS, 399, 1576
Fordham J. L. A., Bone D. A., Read P. D., Norton T. J., Charles P. A., 1989, MNRAS, 237, 513
Fordham J. L. A., Moorhead C. F., Galbraith R. F., 2000, MNRAS, 312, 83
Gehrels N. et al., 2004, ApJ, 611, 1005
Hamann W.-R., Koesterke L., Wessolowski U., 1995, A&AS, 113, 459
Kuin N. P. M., 2014, Astrophysics Source Code Library, record ascl:1410.004
Kuin N. P. M., Rosen S. R., 2008, MNRAS, 383, 383
Kuin N. P. M. et al., 2008, MNRAS, 395, L21
Martin C. et al., 2003, SPIE, 4854, 336
Maselli A. et al., 2014, Science, 343, 48
Mason K. O. et al., 2001, A&A, 365, L36
Mason K. O., Breeveld A., Hunsberger S. D., James C., Kennedy T. E., Roming P. W. A., Stock J., 2004, in Flanagan K. A., Siegmund O. H. W., eds, Proc. SPIE, Vol. 5165, X-Ray and Gamma-Ray Instrumentation for Astronomy XIII. p. 277
McCooke G. P., Sion E. M., 1999, ApJS, 121, 1
Mehdipour M. et al., 2015, A&A, 575A, 22
Niedzielski A., Rochowicz K., 1994, A&AS, 108, 669
Page M. et al., 2013, MNRAS, 436, 1684
Poole T. et al., 2008, MNRAS, 383, 627
Roming P. W. A. et al., 2005, Space Sci. Rev., 120, 95
Shupe D. L., Moshir M., Li J., Makovoz D., Narron R., Hook R. N., 2005, in Shopbell P., Britton M., Ebert R., eds, ASP Conf. Ser. Vol. 347, Astronomical Data Analysis Software and Systems XIV. Astron. Soc. Pac., San Francisco, p. 491
Torres A. V., Massey P., 1987, ApJS, 65, 459
Torres-Dodgen A. V., Massey P., 1988, AJ, 96, 1076
van der Hucht K. A., 2001, New Aston. Rev., 45, 135

This paper has been typeset from a TEX/LATEX file prepared by the author.

Downloaded from http://mnras.oxfordjournals.org/ at NASA Goddard Space Flight Ctr on November 17, 2015